

1 **High-resolution simulations of the plume dynamics in**
2 **an idealized 79°N Glacier cavity using adaptive vertical**
3 **coordinates**

4 **Markus Reinert¹, Marvin Lorenz¹, Knut Klingbeil¹, Bjarne Büchmann²,**
5 **Hans Burchard¹**

6 ¹Leibniz Institute for Baltic Sea Research Warnemünde, Seestr. 15, 18119 Rostock, Germany

7 ²Joint GEOMETOC Support Center, Danish Defence Acquisition and Logistics Organization (DALO),
8 Lautrupbjerg 1-5, 2750 Ballerup, Denmark

9 **Key Points:**

- 10 • Melting of the 79°N Glacier ice tongue by turbulent ocean currents is studied with
11 an idealized 2D-vertical fjord model
- 12 • The role of the meltwater plume as the driver of basal melting is examined together
13 with the influence of environmental factors
- 14 • A high vertical resolution finer than 1 m is achieved in the plume by the use of
15 adaptive vertical coordinates that zoom to stratification

Corresponding author: Markus Reinert, markus.reinert@io-warnemuende.de

Abstract

For better projections of sea level rise, two things are needed: an improved understanding of the contributing processes and their accurate representation in climate models. A major process is basal melting of ice shelves and glacier tongues by the ocean, which reduces ice sheet stability and increases ice discharge into the ocean. We study marine melting of Greenland’s largest floating ice tongue, the 79° North Glacier, using a high-resolution, 2D-vertical ocean model. While our fjord model is idealized, the results agree with observations of the melt rate and the overturning strength. Our setup is the first application of adaptive vertical coordinates to an ice cavity. Their stratification-zooming allows a vertical resolution finer than 1 m in the entrainment layer of the meltwater plume, which is important for the plume development. In a sensitivity study, we show that the buoyant plume at the ice–ocean interface is responsible for the bulk of basal melting. The melting almost stops when the plume has reached neutral buoyancy. There, the plume detaches from the ice tongue and transports meltwater out of the fjord. The detachment depth depends primarily on the ambient ocean stratification. Our results contribute to the understanding of ice–ocean interactions in glacier cavities. Furthermore, we suggest that our modeling approach with stratification-zooming coordinates will improve the representation of these interactions in global ocean models. Finally, our idealized model topography and forcing are close to a real fjord and completely defined analytically, making the setup an interesting reference case for future model developments.

Plain Language Summary

The global increase of sea levels is a consequence of human-induced climate change. It presents a threat to coastal regions and demands action to protect human life and infrastructure near the coast. Planning protective measures requires projections of sea level rise, computed with climate models. We present an approach to improve the simulation of an important contributor to sea level rise: melting of floating ice shelves by ocean circulation. Our modeling approach uses a vertical model grid that evolves over time. The temporal evolution depends on the density structure of the ocean. Large density differences appear just below an ice shelf, where fresh meltwater mixes with salty seawater. The adaptive grid of our model resolves this mixing process in great detail. This is important for an accurate computation of the melt rate and enables us to study in depth the ice shelf–ocean interactions. We study them at the glacier tongue of the 79° North Glacier, which is Greenland’s largest ice shelf. The physical understanding gained from our simulations is also applicable to other floating glacier tongues and ice shelves. We suggest that using the presented model technique in global ocean models can improve projections of melting and sea level rise.

1 Introduction

Sea level rise is a consequence of human-induced climate change and a threat to coastal communities all around the world (IPCC, 2022). To protect human life and infrastructure in coastal areas, measures must be taken, ideally planned well in advance (IPCC, 2022). This requires reliable projections of sea level rise, which depend on the accuracy of climate models as well as on the understanding of the processes contributing to sea level rise. With a contribution of about 20 %, melting of the Greenland Ice Sheet is one of the main processes (Horwath et al., 2022) and the focus of this paper.

The Greenland Ice Sheet, which has the potential to increase sea levels globally by more than 7 m (Aschwanden et al., 2019), discharges into the ocean at so-called outlet glaciers. Some of these glaciers form ice tongues that float on the water and cover their fjords (Straneo & Cenedese, 2015). Greenland’s largest floating glacier tongue is currently the one of the 79° North Glacier (79NG; Schaffer et al., 2020). It is one of the three main outlets of the Northeast Greenland Ice Stream (Schaffer et al., 2017; Kappelsberger et

al., 2021), holding 1.1 m sea-level equivalent of ice (*i.e.*, its ice could lift global sea levels by 1.1 m if melted entirely, Christmann et al., 2021). Schaffer et al. (2020) estimated that 89% of the meltwater leaving the 79NG fjord comes from subglacial melting caused by the ocean. Ice melting on land or at the surface only accounts for the remaining 11% of 79NG meltwater (and even less at other glaciers, see Rignot & Steffen, 2008), which is discharged into the fjord as subglacial runoff at the grounding line. Subglacial melting thins the glacier tongue, which can reduce the buttressing of the ice sheet, *i.e.*, the support of the grounded glacier that is provided by the friction between the ice tongue and the lateral fjord boundaries (Goldberg et al., 2009). With a thinner ice tongue, thus less buttressing, the glacier can flow faster into the ocean, which contributes to sea level rise (Shepherd et al., 2004; Goldberg et al., 2009; Humbert et al., 2022). Furthermore, basal melting can destabilize the ice tongue, which can lead to its breakup (Rignot & Steffen, 2008); in consequence, a lot of ice would be discharged into the ocean (Shepherd et al., 2004). This exemplifies the big role of the ocean in melting the Greenland Ice Sheet (Schaffer et al., 2017) and shows that it is important to understand ice sheet–ocean interactions in glacier fjords like the one at 79° North.

The general idea of ice–ocean interactions under a glacier tongue in Greenland is as follows: Atlantic Intermediate Water (AIW) flows over a sill at the fjord entrance into the glacier cavity as a dense, saline, and warm bottom plume. AIW brings heat into the ice cavity, which is used for melting. The meltwater forms a buoyant plume on the underside of the glacier tongue. This plume causes subglacial melting, transports glacially modified water towards the open ocean, and constitutes the return flow of an overturning circulation within the fjord (Straneo & Cenedese, 2015; Schaffer et al., 2020).

The dense bottom plume and the buoyant subglacial plume are the two main processes in a glacier cavity. However, they are difficult to study, because measurements in Greenland’s fjords are generally sparse (Straneo & Cenedese, 2015), particularly under floating ice tongues, where the ocean is inaccessible to ships and unobservable by satellites. Ice tethered moorings (Lindeman et al., 2020) give some information about processes under the ice, but only at single positions. So numerical models are necessary to gain a detailed understanding of ice sheet–ocean interactions.

A challenge for ocean models is to provide sufficiently high resolution in a glacier fjord to accurately simulate the two plumes. It has been shown that the subglacial plume and particularly its entrainment layer require a vertical resolution of about 1 m or better to correctly model the plume development and the associated melting (Burchard et al., 2022). This is hard to achieve in most ocean models, because of the stark contrast in vertical scales between the fjord depth of several hundred meters and the plume thickness on the order of one to ten meters.

With the vertical coordinates that are commonly used in ocean models, it is unfeasible to achieve a resolution of 1 m along the whole subglacial plume. At 79NG, the plume starts at the grounding line at 600 m depth, so z -coordinate models (Losch, 2008) would require at least 600 vertical layers to resolve the top 600 m of the water column with a 1 m-resolution – much more than can typically be afforded in regional or global models. With σ -coordinates (Timmermann et al., 2012/ed; Gwyther et al., 2020), a high resolution along the whole ice tongue is possible with less layers by activating a zooming towards the ice–ocean interface. However, these terrain-following coordinates have problems when calculating the internal pressure gradient over steep topographic slopes (Haney, 1991; Burchard & Petersen, 1997), which are a typical feature in glacier fjords.

With adaptive vertical coordinates (AVC; Hofmeister et al., 2010), the described problems can be considerably reduced. AVC are terrain-following coordinates that allow with a moderate number of layers a high vertical resolution in places of interest. By minimizing a cost function, AVC adapt automatically to features like stratification, shear, and interfaces (Burchard & Beckers, 2004). This reduces numerical mixing (Klingbeil

118 et al., 2014; Gräwe et al., 2015) and puts more layers in places where more details need
 119 to be resolved, while permitting less vertical resolution in more uniform areas. These co-
 120 ordinates have been used successfully for simulating dense and buoyant plumes in var-
 121 ious conditions (e.g., Umlauf et al., 2010; Chegini et al., 2020), but not yet for glacier
 122 fjord modeling. We will show that the stratification-zooming feature of AVC is very use-
 123 ful for modeling the ocean circulation under ice shelves, because this provides a high ver-
 124 tical resolution of 1 m in the subglacial plume and the bottom plume with feasible com-
 125 putational cost.

126 We created an idealized 2D-vertical simulation of the 79NG fjord using AVC to-
 127 gether with a melt parametrization (Burchard et al., 2022) that is suitable for high ver-
 128 tical resolution at the ice–ocean interface. To our knowledge, this is the first model to
 129 use stratification-zooming coordinates like AVC in a glacier cavity. In addition to test-
 130 ing the performance of AVC under an ice tongue, we use our model to study the sensi-
 131 tivity of the 79NG system to environmental influences. The 20 scenarios of our sensi-
 132 tivity study analyze the effect of the salinity and temperature stratification of the am-
 133 bient ocean, test the importance of the subglacial discharge, examine the role of the sill,
 134 and investigate the influence of roughness or smoothness of the ice tongue.

135 This paper is organized as follows. The following Section 2 describes our model setup,
 136 compares it to the real 79NG fjord, explains our modeling choices including AVC, and
 137 describes our analysis methods. Section 3 shows the results of our default simulation (Sec-
 138 tion 3.1), the performance of AVC (Section 3.2), and the results of our sensitivity study
 139 (Section 3.3). This is followed in Section 4 by a discussion of the physical processes we
 140 observe in all our numerical experiments and what we learn from these findings about
 141 ice–ocean interactions in glacier cavities. We also discuss the role of AVC in obtaining
 142 the presented results. Some conclusions and an outlook are given in Section 5. Appendix
 143 A lists the mathematical expressions used to build our idealized setup, so that our model
 144 can serve as a reference test case for future model developments.

145 2 Methods

146 2.1 Idealized 2D model of the 79°N Glacier fjord

147 We built an idealized numerical ocean model of the 79° North Glacier (79NG) fjord
 148 located in Northeast Greenland, using GETM, the General Estuarine Transport Model
 149 (Burchard & Bolding, 2002). This model is suitable for our purpose, because

- 150 1. GETM comes with adaptive vertical coordinates (AVC) that allow high vertical
 151 resolution in areas of interest for low computational cost (Section 2.3);
- 152 2. GETM includes state-of-the-art vertical turbulence closure with GOTM (Burchard
 153 et al., 1999; Umlauf & Burchard, 2005; Li et al., 2021);
- 154 3. GETM has been developed specifically for the coastal ocean and estuaries (Klingbeil
 155 et al., 2018).

156 A glacier fjord is a special type of estuary, in which the subglacial discharge plays the
 157 role of a river in a classical estuary (Straneo & Cenedese, 2015; Muilwijk et al., 2022).
 158 However, the main source of freshwater is not the subglacial discharge, but the subglacial
 159 melting of the floating ice tongue (Schaffer et al., 2020). Since this is the first time that
 160 GETM is used for simulating a glacier fjord, we extended the model to include ice tongues
 161 and basal melting. The details of this new GETM feature are explained in Section 2.2.

162 Our GETM setup is a two-dimensional (x, z) representation of the 79NG fjord, of
 163 which we consider the main glacier terminus, without the adjacent Dijnphna Sund (Fig. 1a).
 164 The ice tongue of 79NG is about 75 km long and 20 km wide; our model has the same
 165 width ($L_y = 20$ km) and twice the length ($L_x = 150$ km), to have a sufficiently large

166 “buffer” between the glacier cavity – which is our main interest – and the open ocean
 167 boundary. We resolve the domain with 300 water columns in x -direction ($\Delta x = 500$ m)
 168 and one grid point in y -direction; the resolution in z -direction with 100 adaptive layers
 169 is explained in Section 2.3. At this horizontal resolution, neither nonhydrostatic effects
 170 associated with the plumes nor nonhydrostatic internal waves are resolved, so it is ap-
 171 propriate to use GETM in hydrostatic mode (Klingbeil & Burchard, 2013).

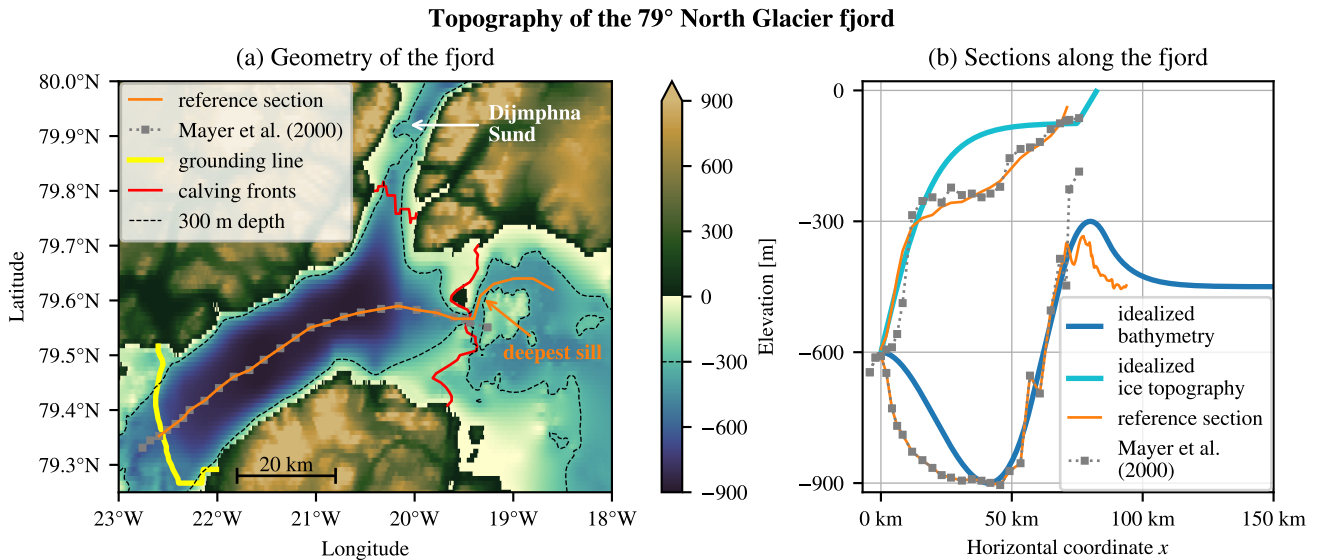


Figure 1. (a) Map of the 79NG fjord and its surroundings showing the bottom elevation from the RTopo-2.0.4 dataset (Schaffer et al., 2019, resolution $30'' = 1/120^\circ$) together with the positions of seismic depth soundings by Mayer et al. (2000). The floating ice-tongue extends from the grounding line in the Southwest to the northern calving front in the Dijmphna Sund and to the main calving front in the East. Atlantic water must pass over a 325 m-deep sill (labeled deepest sill) to flow from the open ocean into the cavity. The reference section is a path from the grounding line towards the open ocean that follows the depth soundings up to the calving front and passes over the deepest sill. (b) Bathymetries and ice topographies along the reference section (from RTopo), along the section by Mayer et al. (2000), and in our idealized 2D fjord model. Note that the deepest sill is the shallowest point along the reference section. The sill depth in our default setup (b) is 300 m, shown as a thin dashed contour in (a).

172 To construct the bottom topography of our idealized 79NG model, we look at two
 173 datasets (Fig. 1). The seismic depth soundings by Mayer et al. (2000) are the most ac-
 174 curate measurements of the bathymetry in the part of the fjord that is covered by the
 175 ice tongue. The retreat of the ice tongue in recent decades facilitated more detailed bathymetry
 176 measurements near the fjord entrance. In their bathymetric survey, Schaffer et al. (2020)
 177 showed that the fjord is separated from the open ocean by a sill that is 325 m deep on
 178 its deepest point. Since this sill depth is not representative for the whole width of the
 179 fjord (Fig. 1a), we use a shallower sill in our idealized 2D model (Fig. 1b). It is at 300 m
 180 depth in our default setup; in our sensitivity study, we analyze the effect of the sill by
 181 varying its depth from 200 m to 450 m (Section 3.3.4).

182 The bathymetry of our idealized model is a smooth concatenation of simple, an-
 183 alytical functions (Fig. 1b): A third-order polynomial connects the grounding line (600 m
 184 depth) with the deepest point in the trough (900 m) and continues until it reaches a slope

185 of 2.5 %. It is then connected linearly to the parabola forming the sill with its maximum
 186 (300 m) at 80 km from the grounding line. The parabolic sill goes over into an exponen-
 187 tially decreasing shelf that converges towards a depth of 450 m far offshore. The math-
 188 ematical details are given in Appendix A1. In our sensitivity experiment without a sill,
 189 the linear slope is directly connected with the exponential shelf. Apart from the sill, our
 190 model bathymetry only differs markedly from the measured section between the ground-
 191 ing line and the trough (Fig. 1b). Despite this difference, we think that a simpler bathymetry
 192 with fewer parameters is preferable to a perfect fit to a single transect for an idealized
 193 model such as ours. Also, this deep part of the fjord is mostly inactive in our simulations.

194 At the grounding line, which forms the left/western boundary of our model ($x =$
 195 0), subglacial discharge enters the glacier fjord. This runoff is implemented in our GETM
 196 setup like river input. It is added as freshwater at the local freezing point (-0.45°C , which
 197 is less than 0°C due to pressure) to the first water column. We take a constant discharge
 198 rate of $70\text{ m}^3\text{ s}^{-1}$ (equivalent to 0.07 mSv reported by Schaffer et al., 2020) in our default
 199 setup and varied this value in our sensitivity study (Section 3.3.3). The discharge is dis-
 200 tributed uniformly over the whole water column, which is about 6.3 m thick at the first
 201 grid center.

202 At the open boundary on the right/eastern end of our model domain ($x = L_x =$
 203 150 km), we prescribe the surface elevation η and the ambient ocean stratification. For
 204 the former, we use a constant zero elevation. We also tested forcing the model with an
 205 M2 tidal oscillation of 0.5 m -amplitude, as measured by Christmann et al. (2021), but
 206 our experiments showed that the melt rate is relatively unaffected by the tidal forcing.
 207 Therefore, the tide is neglected in the present study. Regarding the open boundary strat-
 208 ification, we use idealized and constant-in-time profiles of temperature and salinity. They
 209 are specified by T - and S -values at sea level, at 100 m depth, and at 300 m depth (shown
 210 in Fig. 2 and listed in Appendix A3), using linear interpolation in between and constant
 211 extrapolation below. In our default setup, the resulting profiles are close to CTD mea-
 212 surements by Schaffer et al. (2020), see the comparison in Fig. 2. We also perform a sen-
 213 sitivity study with modified stratifications (Sections 3.3.1 and 3.3.2).

214 The model is initialized at rest with a homogeneous stratification equal to the strat-
 215 ification at the open boundary. We run the model with a timestep for the barotropic mode
 216 of $\Delta t = 5\text{ s}$, in accordance with the CFL stability criterion, demanding $\Delta t \leq \Delta x / \sqrt{gH_{\max}} \approx$
 217 5.3 s (using $H_{\max} = 900\text{ m}$ as the maximum depth of the fjord, see Fig. 1, ignoring the
 218 ice cover). We use a split factor of $M = 3$, so that the baroclinic mode is computed ev-
 219 ery $\Delta t_{3\text{D}} = M\Delta t = 15\text{ s}$. While our default setup can be run with a larger baroclinic
 220 timestep, the high-melt scenarios give smoother results with a higher temporal resolu-
 221 tion, so we decided to use this split factor for all our runs. We activated divergence damp-
 222 ing with a diffusion of $A_n = 50\text{ m}^2\text{ s}^{-1}$ on barotropic transports for a conservative smooth-
 223 ing of the sea surface (Vallis, 1992). After a few simulation months, our model approaches
 224 a quasi-steady state, in which melting and circulation are almost time-independent. The
 225 results shown in this paper are 24 h-averages taken at the end of a six-month simulation
 226 and represent the steady state.

227 2.2 Implementation of glacier ice in GETM

228 For this study, we added a new feature to GETM that allows simulations of glacier
 229 fjords covered by an ice tongue. Where the ice tongue is present, it adds additional pres-
 230 sure (Section 2.2.1), friction (Section 2.2.2), and melt fluxes (Section 2.2.3) to the sea
 231 surface. Our implementation allows the ice to move freely vertically, for example with
 232 long waves, but it is fixed horizontally. Calving is not included in our model.

233 In this paper, we use the term *sea surface* to refer to the (moving) upper bound-
 234 ary of the ocean, denoted $\eta = \eta(x, t)$ and measured from $z = 0$ with positive values
 235 upwards. Depending on the x -position, the sea surface can be the ice–ocean interface or

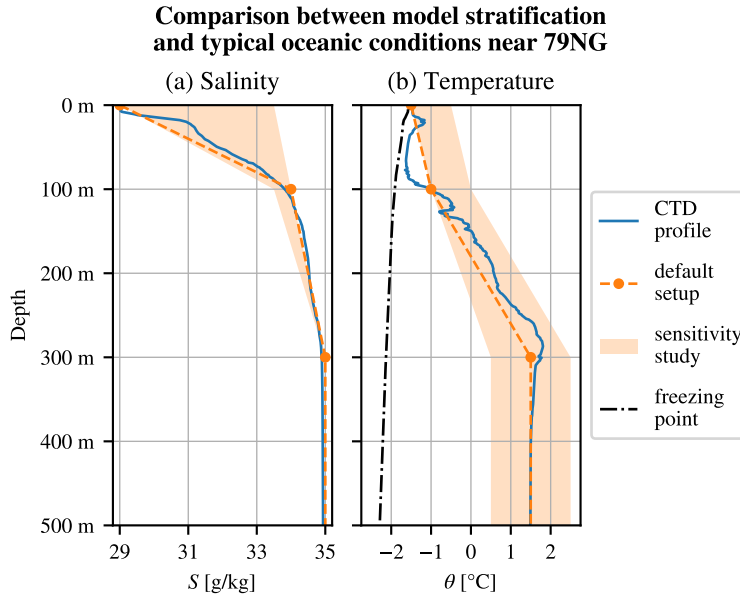


Figure 2. Stratification used in our model as boundary and initial conditions compared with salinity (a) and temperature (b) measurements near the 79NG fjord. The shaded area marks the minimum and maximum values tested in our sensitivity study. The CTD profile was taken in 2017 on RV *Polarstern* (Kanzow et al., 2018) and represents a typical ambient ocean stratification for 79NG (Schaffer et al., 2020, see their Fig. 1a for the location of the profile). The freezing point of saline water in (b) corresponds to the shown CTD profile. We used the Python package *gsw* (TEOS-10; IOC et al., 2010) to convert pressure to depth and to compute the freezing temperature.

236 the atmosphere–ocean interface. Furthermore, we use the term *sea level* to refer to the
237 level $z = 0$, which is the initial position of the atmosphere–ocean interface.

2.2.1 Pressure due to ice and initial sea surface elevation

239 Under glacier ice, the pressure at the ice–ocean interface is the atmospheric pres-
240 sure (constant in our model) plus the contribution from the weight of the ice tongue (Losch,
241 2008). We can represent this pressure due to floating ice as $p_i = g\rho_i h_i$, where h_i is the
242 thickness of the ice column and ρ_i its (homogeneous) density (Table 1). Both $h_i(x)$ and
243 ρ_i are constant-in-time in our implementation and serve as input parameters to the model.

244 To initialize our model in an equilibrium state, we must prescribe the initial sur-
245 face elevation $\eta_0 = \eta(t = 0)$ such that the ocean with the floating glacier ice is in hy-
246 drostatic balance. This is the case if the water displaced by the ice tongue has the same
247 weight as the ice tongue (Archimedes’ principle). For an initially homogeneous strati-
248 fication with (water) density $\rho(z)$, this condition can be expressed as:

$$249 \quad \rho_i h_i = \int_{\eta_0}^0 \rho(z) dz. \quad (1)$$

250 In our setup, we prescribe the lower ice edge η_0 (see below) and determine h_i such that
251 (1) is fulfilled, which has the consequence that we have slightly different ice thicknesses
252 h_i for different stratifications $\rho(z)$ (difference to the default setup is always less than 20 cm).
253 Note that a corollary of (1) is the handy rule-of-thumb $\eta_0 \approx -0.9h_i$, which says that
254 90% of an ice column is below sea level and 10% is above.

Table 1. Settings and parameters of our model in the default scenario

Name of the parameter	Symbol	Value
Geometry:		
length of the fjord	L_x	150 km
width of the fjord	L_y	20 km
roughness length of the sea floor	z_0	1.5×10^{-3} m
roughness length of the ice tongue	$z_{0,\text{ice}}$	1×10^{-2} m
Glacier:		
ice temperature	T_i	-20 °C
ice density	ρ_i	920 kg m^{-3}
subglacial discharge		$70 \text{ m}^3 \text{ s}^{-1}$
Numerics:		
vertical model layers		100
horizontal resolution	Δx	500 m
barotropic timestep	Δt	5 s
baroclinic timestep	Δt_{3D}	15 s
divergence damping	A_n	$50 \text{ m}^2 \text{ s}^{-1}$
Thermodynamics:		
heat capacity of sea water	c	$3985 \text{ J kg}^{-1} \text{ K}^{-1}$
heat capacity of glacial ice	c_i	$1995 \text{ J kg}^{-1} \text{ K}^{-1}$
latent heat of fusion	L_i	$3.33 \times 10^5 \text{ J kg}^{-1}$

255 Given the initially horizontally homogeneous (and stable) ocean stratification, we
256 initialize the ice in its equilibrium position by evaluation of the integral in (1). As the
257 simulation runs, the stratification changes due to basal melting, subglacial discharge, am-
258 bient water inflow, and mixing, so the equilibrium position of the ice changes as well. Since
259 the ice in our model can move freely vertically with the convergence and divergence of
260 transports, it will adapt to the changing stratification. The setups presented here reach
261 a quasi-steady state, in which the glacier tongue has found a new equilibrium position,
262 which is slightly (on the order of millimeters) different from the initial position.

263 In our idealized 79NG fjord model, we prescribe a smooth ice–ocean interface be-
264 tween the grounding line at 600 m depth and the calving front at $x = 75$ km, where the
265 ice–ocean interface is 75 m below sea level. For the idealized ice shape, we choose a hy-
266 perbolic tangent with a maximum slope of 2.5 % at the grounding line (see Appendix A2
267 for the mathematical details). This fits well with the measured ice slope near the ground-
268 ing line (see the reference section in Fig. 1b). Since subglacial melting is strongest in this
269 area (Schaffer et al., 2020), we believe it is important to reproduce the ice topography
270 well near the grounding line and accept that the idealized shape differs from observa-
271 tions at mid-depths, as we prefer a simple, analytical ice shape over a perfect fit to a sin-
272 gle transect.

273 At the calving front, a big slope is to be avoided, as it would cause problems with
274 the terrain-following coordinates, because the water near the calving front is strongly strat-
275 ified, so individual grid cells would span a large density range. Therefore, we extend the
276 ice–ocean interface with a linear 1 %-slope until sea level is reached. We also tested higher
277 slopes at the calving front, but the model results were poorer, because the horizontal flow
278 below the calving front was too much diluted by passing through too many cells. Thus,
279 we use a slope instead of a vertical wall at the calving front. This is a deviation from the
280 real system, but an acceptable one, since our focus lies on processes inside the glacier
281 cavity, which are not much affected by this difference.

282

2.2.2 Surface friction

283

284

285

286

287

Where the ocean is covered by glacier ice, there is a no-slip boundary condition at the sea surface (Burchard et al., 2022). This friction at the ice–ocean interface is implemented in GETM according to the law-of-the-wall with a roughness length $z_{0,\text{ice}}$, similar to bottom friction. In our default scenario, we use the value $z_{0,\text{ice}} = 0.01$ m. The effects of smoother or rougher ice are tested in our sensitivity analysis (Section 3.3.5).

288

2.2.3 Parametrization of subglacial melting

289

290

291

292

293

294

295

We implemented the subglacial melt formulation by Burchard et al. (2022). This parametrization, based on the three-equation model (D. M. Holland & Jenkins, 1999), is suitable for high vertical resolutions under the ice. In our free-surface model, meltwater is added like precipitation as a real freshwater flux (Huang, 1993) to the uppermost grid cell of the water column with a melt rate v_b (in ms^{-1}). There is no salt flux, $f_b^S = 0$, because the melted glacier ice is assumed to have zero salinity. There is, however, a temperature flux at the ice–ocean interface:

296

$$f_b^T = v_b \left[\frac{c_i}{c} (\theta_b - T_i) + \frac{L_i}{c} - \theta_b \right]. \quad (2)$$

297

298

299

300

301

302

303

304

In the squared bracket, the first term corresponds to the energy necessary for heating up the glacial ice from its core temperature T_i to the melt layer temperature θ_b ; the second term is the latent heat of the phase change from ice to water; the last term appears because water is exchanged between ice and ocean, *i.e.*, the ice–ocean interface is a non-material interface in our model (Jenkins et al., 2001). The values of the constants in (2) are given in Table 1. The melt layer is a thin layer at the ice–ocean interface, that is not resolved but parametrized in our model. For a detailed discussion, see Burchard et al. (2022).

305

306

307

308

309

310

311

312

313

314

315

The here-described implementation of melting differs from that used by Burchard et al. (2022), because their 1D model has a rigid lid. In a rigid lid model, the water volume cannot increase, so a virtual salt flux through the ice–ocean interface is needed to get the diluting effect of basal melting on salinity, and a virtual temperature flux is needed instead of (2). However, the more realistic approach is adding meltwater explicitly (Huang, 1993; Jenkins et al., 2001), without a salt flux and with only a real temperature flux, as we do it in this study. Even though melting increases the water volume in our model, the ice volume does not decrease. To allow for a decreasing ice volume and a thinning ice tongue, ice dynamics would have to be modeled as well. Instead, we assume that there is a balance between basal melting of the ice tongue and the discharge of glacier ice from land into the ocean.

316

2.3 Adaptive vertical coordinates

317

318

319

320

321

322

323

324

325

326

Our GETM setup uses adaptive vertical coordinates (AVC) described by Burchard and Beckers (2004) and Hofmeister et al. (2010). These coordinates are well-suited for representing surface-attached buoyant plumes (Chegini et al., 2020) and dense bottom currents (Hofmeister et al., 2010; Umlauf et al., 2010). AVC are topography-following coordinates, in which the vertical distribution of the model layers changes with time. The temporal change of model layers is implemented by minimizing a cost function depending on the model state, particularly the stratification. The coordinates adapt in a way that there are more layers in regions with higher stratification. This ensures high vertical resolution in areas of strong vertical density gradients and minimizes numerical mixing (Hofmeister et al., 2010; Klingbeil et al., 2014; Gräwe et al., 2015).

327

328

329

In the 79NG fjord, important density differences exist in two locations: (i) Between the meltwater plume at the ice–ocean interface and the ambient water below, and (ii) between the bottom current and the cavity water above (Schaffer et al., 2020). With AVC

330 we can obtain high resolutions in both of these plumes and particularly in their entrain-
 331 ment layers, without a large increase in computational cost ($< 10\%$ more computation
 332 time compared to σ -coordinates). For this, we configured AVC so that they zoom towards
 333 stratification and towards the sea surface. An explicit bottom-zooming is not required,
 334 because the stratification-zooming itself provides sufficiently high resolution in the bot-
 335 tom plume (Section 3.2). Activating the zooming towards the seafloor would also result
 336 in high resolution in the deep trough of the glacier fjord and on the continental shelf out-
 337 side the ice cavity, even though these parts are mostly inactive in our simulations. Thus,
 338 we do not activate it and opt instead for an even higher resolutions near the ice–ocean
 339 interface, which is important for the accurate representation of melting (Burchard et al.,
 340 2022). While 50 coordinate levels would be sufficient to achieve a vertical resolution bet-
 341 ter than 2 m in the plume under the ice, we present in this paper simulations with 100
 342 AVC layers to show the plumes and the circulation in great detail.

343 2.4 Analysis of plume-averaged quantities

344 To analyze the entrainment of the subglacial plume, we compute its bulk proper-
 345 ties, *i.e.*, the vertically averaged plume characteristic. We want to diagnose the bulk val-
 346 ues following the ideas by Arneborg et al. (2007) in the modified form for plumes un-
 347 der ice shelves (Burchard et al., 2022):

$$348 \quad \bar{b}D = \int_{-\infty}^{\eta} b(z) dz, \quad (3)$$

$$349 \quad \bar{b}D^2 = 2 \int_{-\infty}^{\eta} b(z)z' dz, \quad (4)$$

$$350 \quad \bar{u}D = \int_{-\infty}^{\eta} u(z) dz, \quad (5)$$

351 where $z' = \eta - z$ is the distance from the ice–ocean interface, $b(z) = -g[\rho(z) - \rho_0]/\rho_0$
 352 is the buoyancy, and ρ_0 is the ambient ocean density. However, the above equations have
 353 been derived in a 1D setting with the assumptions that the ambient water below the plume
 354 is homogeneous (with density ρ_0) and stagnant ($u = 0$), which is not the case in our
 355 2D model. So an integration to $-\infty$ or to the sea floor at $z = -H$ would not make sense,
 356 because it would include several different water masses in the plume analysis. Instead,
 357 we choose an integration depth $h_0 > 0$, consider the water mass at $z = \eta - h_0$ as the
 358 ambient water, and use the following modified formulas

$$359 \quad \bar{b}D = \int_{\eta-h_0}^{\eta} b(z) dz, \quad (6)$$

$$360 \quad \bar{b}D^2 = 2 \int_{\eta-h_0}^{\eta} b(z)z' dz, \quad (7)$$

$$361 \quad \bar{u}\bar{b}D = \int_{\eta-h_0}^{\eta} u(z)b(z) dz, \quad (8)$$

362 as definitions of plume thickness D , plume buoyancy \bar{b} , and plume velocity \bar{u} . Note that
 363 dividing (7) by (6) gives D , dividing (8) by (6) gives \bar{u} , and dividing (6) by D gives \bar{b} .
 364 We take as ρ_0 the density linearly interpolated from cell centers to $z = \eta - h_0$; a ver-
 365 tical interpolation gives considerably smoother graphs for the bulk values than taking
 366 the density of the grid cell containing $z = \eta - h_0$. The factors of $b(z)$ and \bar{b} in (8) en-
 367 sure that the integral gives more weight inside the plume than outside, where $b(z)$ is smaller
 368 since the local density $\rho(z)$ is closer to that of the ambient water, ρ_0 . We use velocities
 369 horizontally interpolated to cell centers (instead of cell interfaces) in (8), so that all bulk
 370 values are defined on cell centers.

The bulk values of velocity \bar{u} , buoyancy \bar{b} , and thickness D allow to compute the Froude number

$$\text{Fr} = \frac{|\bar{u}|}{\sqrt{|\bar{b}|D}}, \quad (9)$$

which is a non-dimensional number relating the velocity of the plume to the phase speed of long waves at the plume interface (Arneborg et al., 2007; Burchard et al., 2022). The Froude number tells us whether the flow is supercritical ($\text{Fr} > 1$) or subcritical ($\text{Fr} < 1$).

Following P. R. Holland and Feltham (2006), the bulk values can be used to formulate a conservation equation for the plume volume:

$$\partial_t D + \partial_x(D\bar{u}) + \partial_y(D\bar{v}) = v_b + v_e, \quad (10)$$

where the terms on the right-hand side are the melt rate v_b and the entrainment velocity v_e . For our 2D system ($\partial_y = 0$) in steady state ($\partial_t = 0$), (10) implies

$$\bar{u}\partial_x D = -D\partial_x \bar{u} + v_b + v_e, \quad (11)$$

which means that the plume thickness increases in x -direction by flow convergence ($-D\partial_x \bar{u}$), melting, and entrainment. Since the melting is computed by our numerical model, we can reformulate (11) to diagnose the entrainment (Burchard et al., 2022):

$$v_e = D\partial_x \bar{u} + \bar{u}\partial_x D - v_b. \quad (12)$$

The choice of the integration depth h_0 requires some considerations. It must be chosen such that (as long as the plume is attached to the ice) $z = \eta - h_0$ lies always outside the plume in a weakly stratified region, but not too far away, so that $\rho_0 = \rho(z = \eta - h_0)$ is actually the density of the water surrounding the plume. To find a suitable integration depth, a visual inspection of the model result is helpful. The identified value is a good choice if the computed bulk values are stable, *i.e.*, they do not vary much for small variations of h_0 . In our default scenario, this is the case for $h_0 = 10$ m. However, the precise choice of h_0 is not critical for the results.

For the analysis of the dense bottom plume, we use an analogous approach, but with integration from the sea floor at $z = -H$ to $z = -H + h_0$, and with $z' = H + z$ being the distance from the sea floor in (7). We take $h_0 = 20$ m as the integration height for the bottom plume, since its typical thickness is around two-times that of the subglacial plume.

2.5 Analysis of the overturning circulation

A key property of a glacier fjord is the strength of its overturning circulation, often reported in milli-Sverdrup ($1 \text{ mSv} = 1000 \text{ m}^3 \text{ s}^{-1}$). We take as a measure of the overturning strength the maximum (in absolute value) of the (volume) stream function over the sill ($x = 80$ km). The stream function ψ is defined by

$$\partial_z \psi = uL_y, \quad (13)$$

$$\partial_x \psi = -wL_y, \quad (14)$$

and the condition that $\psi = 0$ on the sea floor; L_y is the (constant) width of the fjord (Table 1). Numerically, we diagnose ψ by summing the horizontal transports $u\Delta zL_y$ (defined on cell edges) from the sea floor to the sea surface, which follows from (13) and naturally satisfies $\psi = 0$ at the bottom. Then (14) is automatically fulfilled thanks to the 2D continuity equation, $\partial_x u + \partial_z w = 0$. Since the model results shown in this paper are in steady state, the contour lines of the stream function ψ are trajectories.

3 Results

In this section, we present at first the steady state of our default scenario (Sections 3.1 and 3.2), then we perform a sensitivity study with varying physical parameters (Section 3.3).

3.1 Circulation and melting in the default scenario

In our default model setup, which is an idealized representation of the present day situation at 79NG as observed by Schaffer et al. (2020), we find an estuarine-like circulation in the glacier cavity (Fig. 3a–d). This circulation is made up of two gravity plumes: strong, turbulent, and focused currents that are driven by density differences. One is a buoyant plume at the lower ice edge, driving the melting of the ice tongue and transporting glacially modified water out of the fjord into the ambient ocean (blue in Fig. 3a). The other plume – a dense bottom current – brings warm and salty Atlantic Intermediate Water (AIW) from the open ocean over the sill into the glacier cavity (red in Fig. 3a). The strength of the overturning circulation is 39 mSv (Fig. 3b), consistent with the value of (46 ± 11) mSv obtained from hydrographic measurements (Schaffer et al., 2020).

Subglacial melting creates a layer of cold water just below the ice along the whole glacier tongue (Fig. 3c). This meltwater is transported away from the glacier and introduces a layer of cold water into the ambient ocean at depths of around 90 m to 95 m below sea level. Minimum temperatures offshore the calving front are below -1.5°C at 94 m depth. Apart from this layer and its immediate surroundings, the temperature stratification offshore the sill is mostly in equilibrium with the imposed open ocean conditions. As the flow of AIW from the open ocean into the glacier cavity is hindered by the sill, the cavity water becomes colder than the open ocean water by mixing with meltwater (inset of Fig. 3c).

Salinity differences are the main drivers of the circulation in the 79NG fjord (Fig. 3d). On the one side, the subglacial plume rises along the ice tongue because it is fresher, thus lighter than the water inside the cavity. On the other side, AIW flows down the bottom slope into the glacier cavity because it is saltier, thus denser than the cavity water. Comparing the water at the same depth on both sides of the sill, we see that the cavity water, which is a mixture of AIW with meltwater, is at least 0.1 g kg^{-1} fresher than AIW (inset of Fig. 3d). Offshore the sill, the salinity stratification is almost horizontally homogeneous and in equilibrium with the imposed conditions of the open ocean.

Along the whole ice tongue of 79NG, the basal meltrate is positive, *i.e.*, no freezing appears in our simulation (Fig. 3e). We find the strongest melting of 58 m yr^{-1} close to the grounding line and a mostly monotonic decrease of the meltrate afterwards. The meltrate reaches practically zero ($< 0.1 \text{ m yr}^{-1}$) at around 42 km from the grounding line. The rest of the ice tongue has an average meltrate of less than 0.01 m yr^{-1} . The position where the melting stops coincides with the place where the subglacial plume detaches from the ice tongue (see Section 3.1.1). The meltrate averaged over the whole ice tongue is 12.3 m yr^{-1} (corresponding to $20.3 \text{ km}^3 \text{ yr}^{-1}$) in our model, consistent with the value of $(10.4 \pm 3.1) \text{ m yr}^{-1}$, or $(17.8 \pm 5.2) \text{ km}^3 \text{ yr}^{-1}$, estimated by Schaffer et al. (2020) based on measurements. Accordingly, also the percentage of subglacial discharge in the total meltwater production at 79NG is similar between our model (9.8%) and observations (11%; Schaffer et al., 2020). This shows that basal melting is by far the dominant freshwater source in the glacier fjord.

3.1.1 The buoyant subglacial plume

The subglacial plume starts at the grounding line ($x = 0$), where subglacial runoff is discharged into the cavity. Since this discharge is fresher than the water in the fjord, it is positively buoyant and rises along the lower ice edge. We observe in our model that two opposing processes modify the plume water while rising. On its upper side, the plume

Steady state of the 79NG fjord (default scenario)

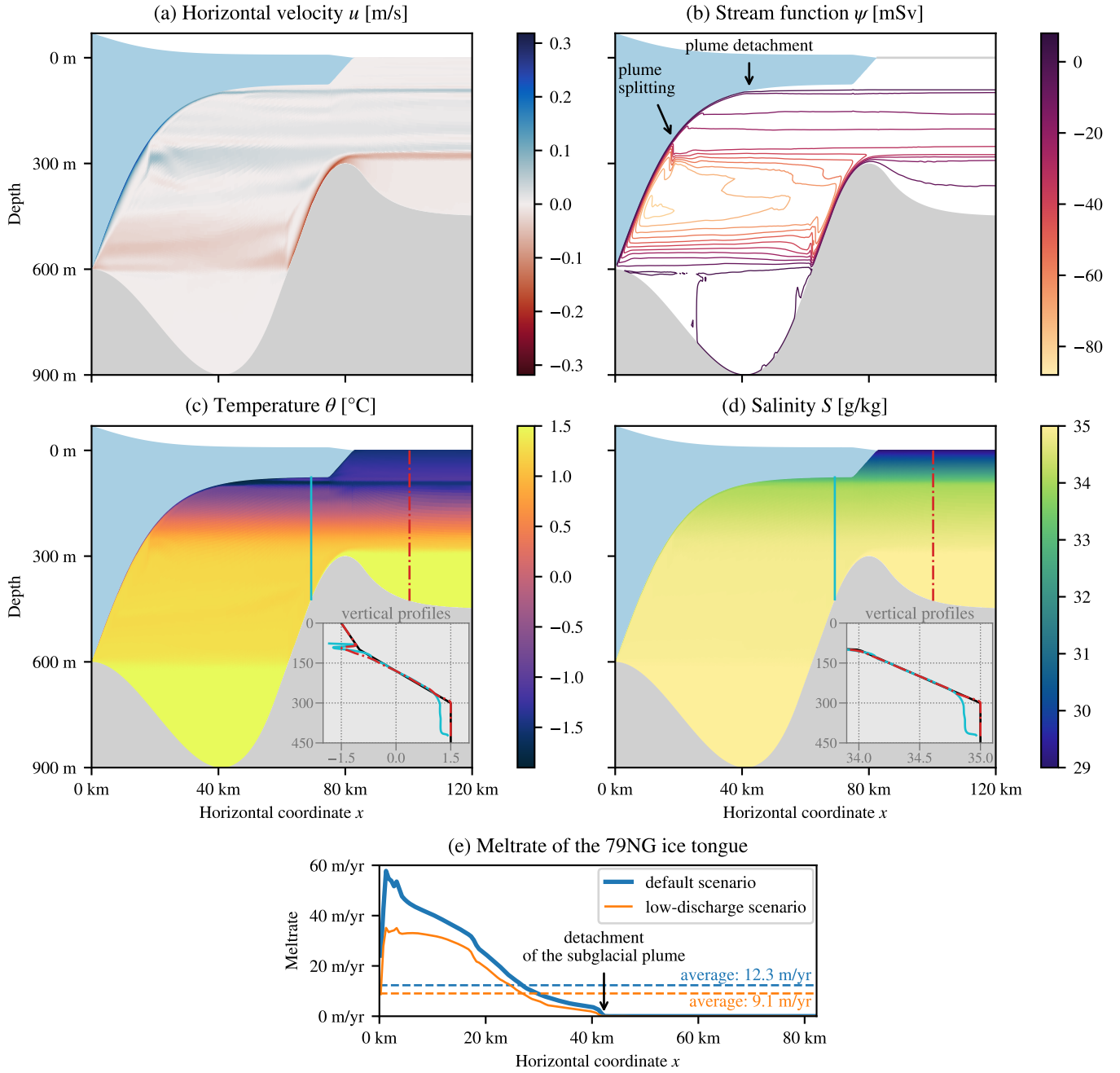


Figure 3. Model results in steady state for our default scenario of the 79NG fjord showing horizontal velocity (a), stream function (b), temperature (c), salinity (d), and meltrate (e). Insets in panels (c) and (d) show vertical profiles of temperature and salinity, respectively, at positions on both sides of the sill marked with vertical lines in the same colors as the graphs; conditions at the open boundary are shown in black for comparison. The thin orange line in panel (e) corresponds to a sensitivity experiment, in which the subglacial discharge is reduced by an order of magnitude compared to the default scenario (Section 3.3.3).

463 causes melting of the ice tongue due to friction, which adds cold and fresh meltwater to
 464 the plume. On its lower side, ambient water is entrained upwards into the plume by tur-
 465 bulent mixing, thus making it saltier and warmer. This way, entrainment transports heat
 466 towards the ice and amplifies the melting (Burchard et al., 2022). As the plume rises,
 467 it passes through ever lighter surrounding water and reaches a point where its density
 468 equals that of the ambient water (Fig. 4a). This is between 95 m and 100 m below sea
 469 level. At this level, the subglacial plume detaches from the ice tongue, propagates hor-
 470izontally away from the glacier, and transports glacially modified water out of the fjord
 471 (Fig. 3a–c).

472 Before this detachment, the plume splits up a number of times. The first splitting
 473 occurs at 18 km from the grounding line (Fig. 5). Until there, the plume was rising through
 474 well-mixed water, allowing it to grow and thicken rapidly by entrainment. However, around
 475 the depth of the sill (300 m), the stratification changes and the ambient water becomes
 476 stably stratified (Fig. 5d). The lower part of the plume consisting of denser water over-
 477 shoots its neutral level, falls about 70 m down, rises slightly again, and finds its neutral
 478 level near $z = -290$ m, where it propagates away from the ice (Fig. 5a,b). This creates
 479 a buoyancy oscillation visible in the streamlines (Fig. 3b). However, the oscillation is strongly
 480 damped, because the plume mixes with ambient water during its ascent and descent (Fig. 5c),
 481 thereby reaching neutral buoyancy quickly (Fig. 5d). Similar though smaller splits of the
 482 plume can be observed several times until the plume detachment. This creates a verti-
 483 cal velocity profile with a number of velocity peaks between the depth of the calving front
 484 and the depth of the sill (Fig. 3a).

485 Prior to the splitting of the plume, its thickness increases from $D = 3$ m at a dis-
 486 tance of 5 km from the grounding line to about $D = 5$ m at $x = 18$ km (Fig. 4a). Over
 487 this distance, the plume becomes more buoyant and increases its vertically-averaged ve-
 488 locity \bar{u} to a maximum of 0.22 m s^{-1} (Fig. 4b,c). When the plume splits, its velocity drops
 489 and so does its buoyancy \bar{b} , because the ambient water below the plume becomes lighter.
 490 After the splitting, the plume thickens more slowly and reaches $D = 6$ m at $x = 40$ km,
 491 just before its detachment from the ice. When it detaches, the plume buoyancy drops
 492 again (Fig. 4c), meaning that the plume density is similar to the ambient density, which
 493 is the reason for the plume detachment. Note that the buoyancy does not go to zero be-
 494 cause the formulas to compute \bar{b} (Section 2.4) are only applicable while the plume is within
 495 10 m from the ice edge; afterwards the thin lines in Fig. 4b–d represent the properties
 496 of the water just below the ice.

497 Entrainment at the plume base is only positive until the plume splits for the first
 498 time (Fig. 6a). The plume thickening afterwards is mainly due to flow convergence (Fig. 6a)
 499 in consequence of the plume slowing down (Fig. 4b). It is not due to entrainment, be-
 500 cause after the initial phase, the entrainment velocity v_e is negative and detrainment ap-
 501 pears (Fig. 6a). So instead of taking up ambient water, the plume in total loses water
 502 to the stratified interior of the cavity (Fig. 3). Correspondingly, the vertical velocity un-
 503 der the plume is negative, *i.e.*, downward (Fig. 6c). The detrained water forms an out-
 504 flowing layer below the plume (Fig. 6b).

505 Our interpretation of the detrainment is that initially, the weakly stratified water
 506 in the deep part of the cavity allows strong turbulence to develop (Fig. 6d), leading to
 507 high entrainment rates of $E = v_e/\bar{u} = \mathcal{O}(2 \times 10^{-4})$ and rapid plume thickening (Fig. 4a),
 508 consistent with the initial plume development and entrainment reported by Burchard
 509 et al. (2022). When the plume arrives in the more stratified upper part of the cavity, the
 510 reduced turbulence is insufficient to sustain the thick plume. Comparing turbulent ki-
 511 netic energy (TKE) in the entrainment part with the detrainment part, we see that in
 512 the latter case, TKE is clearly reduced at the ice–ocean interface, at the plume base, and
 513 below the plume (Fig. 6d). So the turbulence might be too weak to further entrain am-
 514 bient water against gravity, and instead the plume detrains water. This manifests in the
 515 first plume splitting near $x = 18$ km and the subsequent smaller splits as described above.

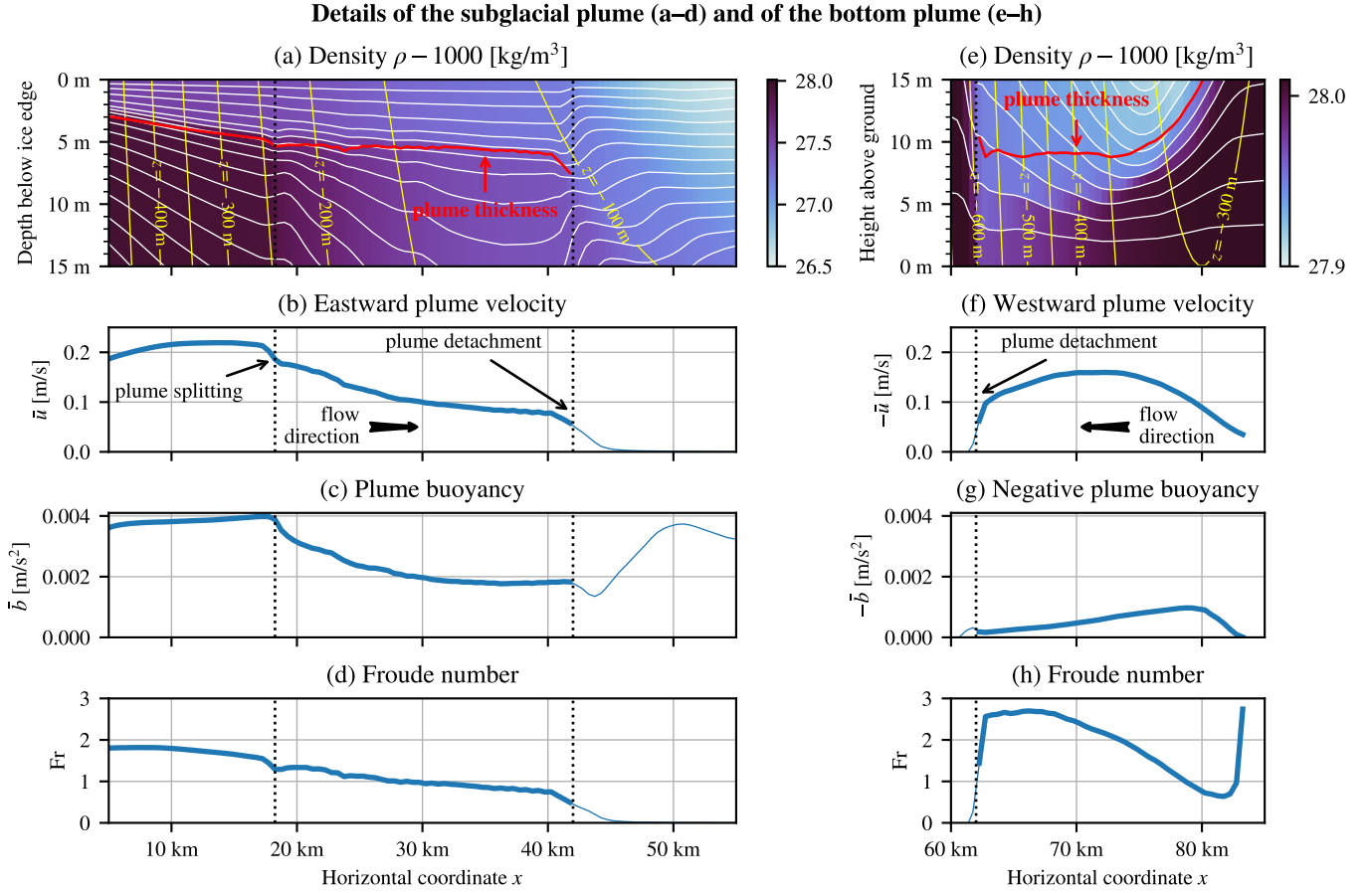


Figure 4. Detailed view of the buoyant plume (a–d) and of the dense plume (e–h) (default scenario). The first row shows density (a) in the 15 m just below the ice–ocean interface and (e) in the 15 m just above the sea floor; note the different starting points of the colorbars. White lines are vertical coordinate levels (cell edges of the model grid) and emphasize the high resolution of about 1 m obtained by AVC in the entrainment layers of both plumes. Depth contours in yellow show that the plume water goes horizontally after the detachment. The red lines represent the thicknesses D of the plumes before their detachments, which are marked by dotted vertical lines. The thicknesses (a,e) and bulk values (b–d,f–h) were calculated as explained in Section 2.4. Note that the bulk values in panels (f) and (g) have opposite signs than those in (b) and (c), because the plumes go in opposite directions and are oppositely buoyant. After the plume detachments, bulk values are shown as thin lines, because they do not represent the plumes anymore; instead, they show the averaged properties of the uppermost 10 m under the ice (b–d) or the lowermost 20 m above the seafloor (f–h).

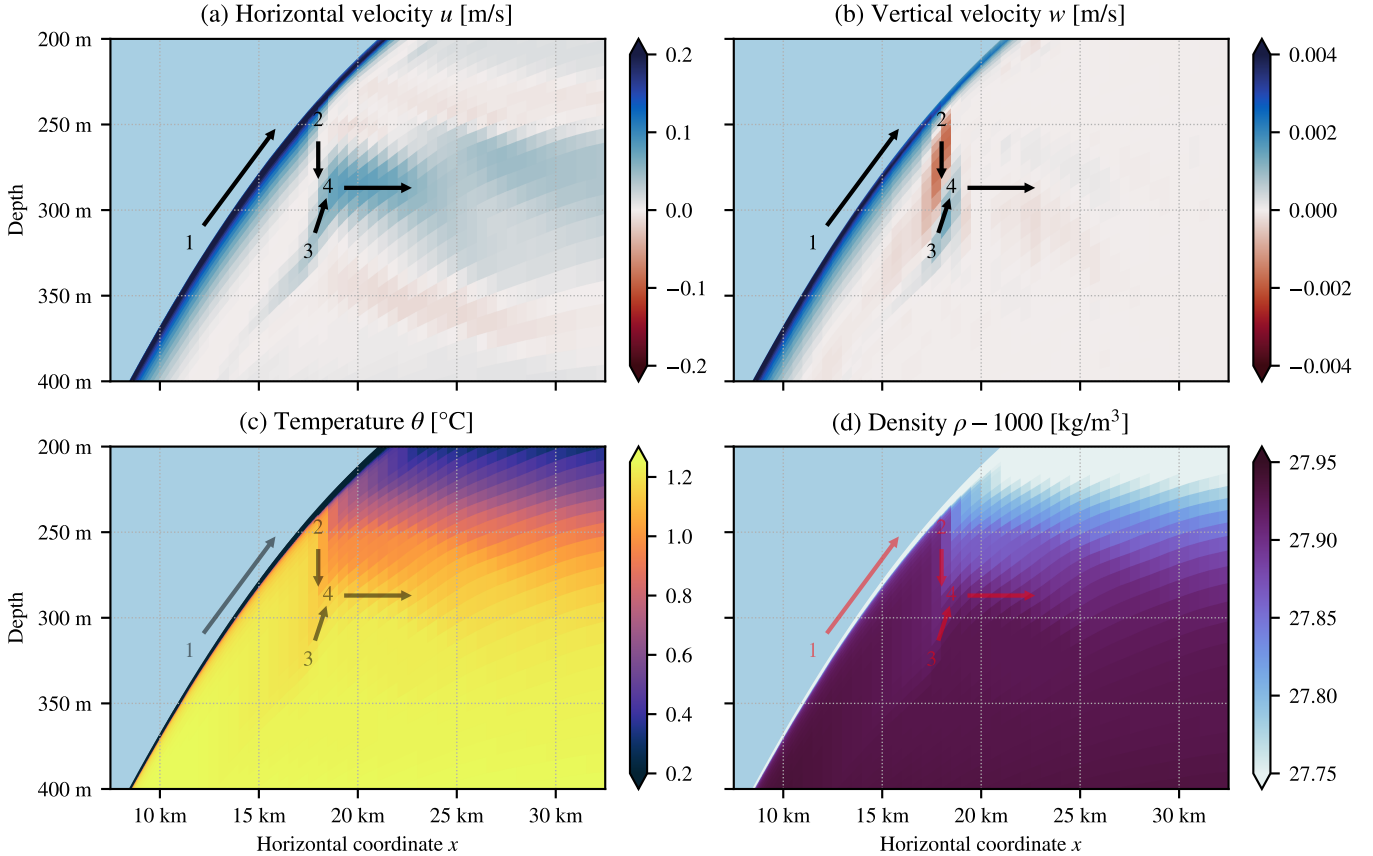
Zoom to the first splitting of the subglacial plume


Figure 5. Zoom to the first splitting of the subglacial plume (default scenario). The arrows represent the flow direction resulting from the combined effects of the horizontal (a) and vertical (b) velocity components: (1) The plume rises along the ice tongue; (2) the lower part of the plume falls down from about 250 m depth to about 320 m depth, while becoming slightly colder and lighter due to mixing with ambient water; (3) the plume rises to about 290 m depth and (4) flows horizontally away from the ice tongue.

516 For most of its path along the ice, the plume is supercritical ($Fr > 1$; Fig. 4d).
 517 It transitions to subcritical flow ($Fr < 1$) around 30 km from the grounding line.

518 *3.1.2 The dense bottom plume*

519 The bottom plume in the 79NG fjord consists of AIW coming from the open ocean.
 520 With a density of 1028.0 kg m^{-3} (Fig. 4e), this is the densest water mass in our system,
 521 as well as the warmest and saltiest (Fig. 3c,d). It flows from the sill at $x = 80 \text{ km}$ down
 522 into the cavity, following the bathymetry. As long as the bottom slope increases, the plume
 523 accelerates up to a vertically-averaged velocity of $\bar{u} = -0.16 \text{ m s}^{-1}$ (Fig. 4f). Due to
 524 this flow divergence, the plume thins from 15 m over the sill to 9 m thickness six kilome-
 525 ter downstream (Fig. 4e).

526 While flowing down the bottom slope, the plume entrains ambient cavity water,
 527 which has a lower density since it contains meltwater (Fig. 4e). In consequence, the plume
 528 density and buoyancy (in absolute value) decrease (Fig. 4g). Similar to the subglacial

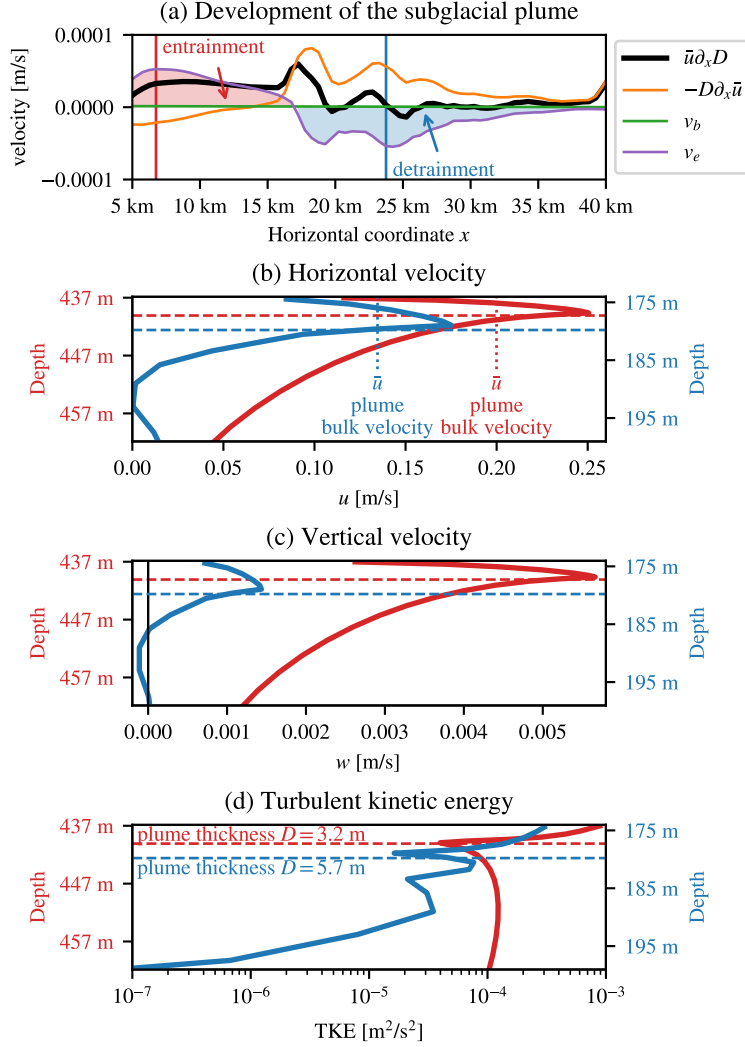


Figure 6. Development of the subglacial plume thickness D before the detachment from the ice tongue, with areas of entrainment and detrainment highlighted (a); vertical profiles at positions near maximum entrainment (red) and detrainment (blue), showing velocity components (b,c) and turbulent kinetic energy (d) in the 25 m under the ice (default scenario). The colored graphs in (a) represent the processes acting on the plume thickness: flow convergence (orange), subglacial melt rate (green, close to zero), and entrainment velocity at the plume base (purple); summed together, they give the thicker black line, see (11). For the calculation of the graphs in (a), plume thickness D and bulk velocity \bar{u} were smoothed with a running average of window size ± 1 km.

529 plume, the bottom plume transports water below its neutral depth. The water then rises
 530 again and adjusts in an oscillating way to its level of neutral buoyancy (Fig. 3b), before
 531 propagating horizontally away from the bathymetry. This way, the bottom plume fills
 532 the cavity with (partially mixed) AIW over a depth range of 450 m to 600 m (Fig. 3a).
 533 At about 600 m below sea level, the plume has detached completely from the bottom.
 534 It cannot propagate further down, because the entrainment of cavity water made the plume
 535 lighter than the water in the trough below 600 m depth. The water in the deep trough
 536 is dense because it consists of almost pure AIW with only little meltwater. This is be-
 537 cause (i) meltwater enters the cavity only at depths where the ice tongue is present, and
 538 (ii) the meltwater is not mixed far below the grounding line (600 m) due to the absence
 539 of strong motion there.

540 The bottom plume is mostly supercritical ($Fr > 1$; Fig. 4h). Only for a short dis-
 541 tance around the peak of the sill, where the bottom plume is slow and thick, the Froude
 542 number is less than one.

543 Outside the cavity, just offshore the sill, even some AIW below the sill level moves
 544 upward and flows over the sill (Fig. 3b). This overflow is driven by an internal pressure
 545 gradient that is vertically homogeneous, since the water on the upstream side of the sill
 546 is unstratified. The phenomenon of upward acceleration of dense water against gravity
 547 is called aspiration and commonly observed in fjords (Inall & Gillibrand, 2010).

548 **3.2 Performance of the adaptive vertical coordinates (AVC)**

549 AVC is one feature of our model that has not been employed before in simulations
 550 of glacier fjords. Our setup uses 100 vertical layers that adapt automatically to the strat-
 551 ification, as explained in Section 2.3. This way, we reach high vertical resolutions in both
 552 plumes.

553 The vertical resolution in the subglacial plume is everywhere close to 1 m and even
 554 better in the entrainment layer at the plume base (white lines in Fig. 4a). Thus, AVC
 555 achieve the necessary resolution to represent the entrainment of the ambient water into
 556 the plume correctly (Burchard et al., 2022). Since the model layers adapt to and follow
 557 the plume, its water is advected mostly along the layers and not across. The plume is
 558 always resolved by five layers or more while it is attached to the ice, which allows to pre-
 559 serve the plume properties well. When the plume detaches from the ice, AVC still man-
 560 age to follow the flow of the meltwater to some extent by partially bending in the hor-
 561 izontal direction (Fig. 4a).

562 The calving front presents a challenge for AVC. As terrain-following coordinates,
 563 they must connect the lower ice edge to the sea level, a difference of 75 m in depth. How-
 564 ever, the flow under the calving front is horizontal and the density is horizontally homo-
 565 geneous, so there is necessarily a divergence between coordinates and plume. By stretch-
 566 ing the calving front over 7.5 km as explained in Section 2.2.1, the vertical position of
 567 the ice–ocean interface changes gradually enough, so that the coordinates manage to adapt
 568 to the plume to some extent and preserve its properties well (see the inset of Fig. 3c).
 569 However, a slight dilution of the plume as it passes under the calving front and through
 570 several layers can still be seen (Fig. 3a–c).

571 Similar to the subglacial plume, also the incoming plume of Atlantic Water is re-
 572 solved by several layers with a thickness on the order of 1 m (Fig. 4e). As the plume prop-
 573 agates down the slope, it thins due to velocity divergence, so the number of layers in the
 574 plume reduces.

575 The high resolution in the vicinity of the ice and the bottom comes at the expense
 576 of thicker layers in the interior of the glacier cavity. While the vertical layers are less than
 577 10 m thick in most areas, there are up to 15 m-thick layers in the middle of the water col-

578 umn in places where the fjord is deepest. However, we believe that this is a good trade-
 579 off, because (i) the thick layers appear in areas where the velocities are small and the
 580 water column is only weakly stratified, and (ii) we obtain very thin layers in the dynam-
 581 ically relevant parts.

582 3.3 Sensitivity studies

583 We now explore how the results change compared to the default scenario for mod-
 584 ified environmental influences. Key properties of all presented scenarios are summarized
 585 in Table 2.

Table 2. Summary of the presented simulations

Scenario	Meltrate (m yr^{-1})	Overturning (mSv)	Runoff
default	12.3	39.2	9.8 %
high salinity	12.6	40.1	9.6 %
low salinity	10.2	32.2	11.6 %
AIW: -1.0 K	7.6	35.1	15.0 %
AIW: -0.5 K	10.0	39.0	11.8 %
AIW: $+0.5$ K	15.5	43.8	8.0 %
AIW: $+1.0$ K	19.0	47.7	6.6 %
PW: $+0.5$ K	12.3	39.3	9.9 %
PW: $+1.0$ K	12.2	38.9	9.9 %
AIW & PW: $+0.5$ K	15.3	42.0	8.0 %
AIW & PW: $+1.0$ K	18.7	47.1	6.7 %
discharge 1/10-th	9.1	25.7	1.5 %
discharge doubled	14.3	49.9	15.8 %
sill at 200 m	9.2	21.7	12.7 %
sill at 250 m	11.1	31.2	10.7 %
sill at 350 m	13.2	57.1	9.2 %
sill at 400 m	13.3	78.1	9.1 %
no sill	13.4	107.2	9.1 %
smooth ice (z0m)	16.1	52.5	7.7 %
rough ice (z0p)	5.6	30.8	19.4 %
Observation	10.4 ± 3.1	46 ± 11	11 %

Meltrate is the subglacial meltrate averaged over the whole ice tongue. Overturning is the strength of the circulation measured above the sill. Runoff is the percentage of subglacial discharge in the total meltwater outflow (discharge plus melting) of the fjord. Observation cites the values reported by Schaffer et al. (2020). AIW stands for (the temperature of) Atlantic Intermediate Water, PW for Polar Water.

586 3.3.1 Influence of the ambient ocean salinity

587 The subglacial plume detaches from the ice tongue and transports meltwater out
 588 of the fjord towards the open ocean at a depth of around 95 m below sea level in our de-
 589 fault scenario. This sensitivity study shows that the depth depends strongly on the salin-
 590 ity stratification of the ambient ocean, which is imposed at the open boundary of the
 591 model. When the salinity of the upper water column is increased, the plume propagates
 592 further along the ice tongue and detaches higher up. With lower salinities above the sill,
 593 the plume does not propagate as far up and detaches earlier.

594 This relation is exemplified by the two sensitivity experiments shown in Fig. 7 in
 595 comparison with the default case. For the high salinity scenario, we increased the sur-
 596 face salinity from 29 g kg^{-1} to 33.5 g kg^{-1} , so that we obtain a linear salinity stratifica-
 597 tion in the upper 300 m of the water column (Fig. 7b). With this stratification, the plume
 598 detaches at around 50 m below sea level (Fig. 7a). In the low salinity case, we kept the
 599 surface value at 29 g kg^{-1} but decreased the salinity at 100 m depth from 34 g kg^{-1} to
 600 33.5 g kg^{-1} (Fig. 7f). Then most of the plume detaches between 125 m and 150 m of depth
 601 (Fig. 7e). These experiments also show that the plume detachment is not caused by the
 602 abruptly changing stratification that is in the default scenario at a similar depth as the
 603 detachment (Fig. 7c,d).

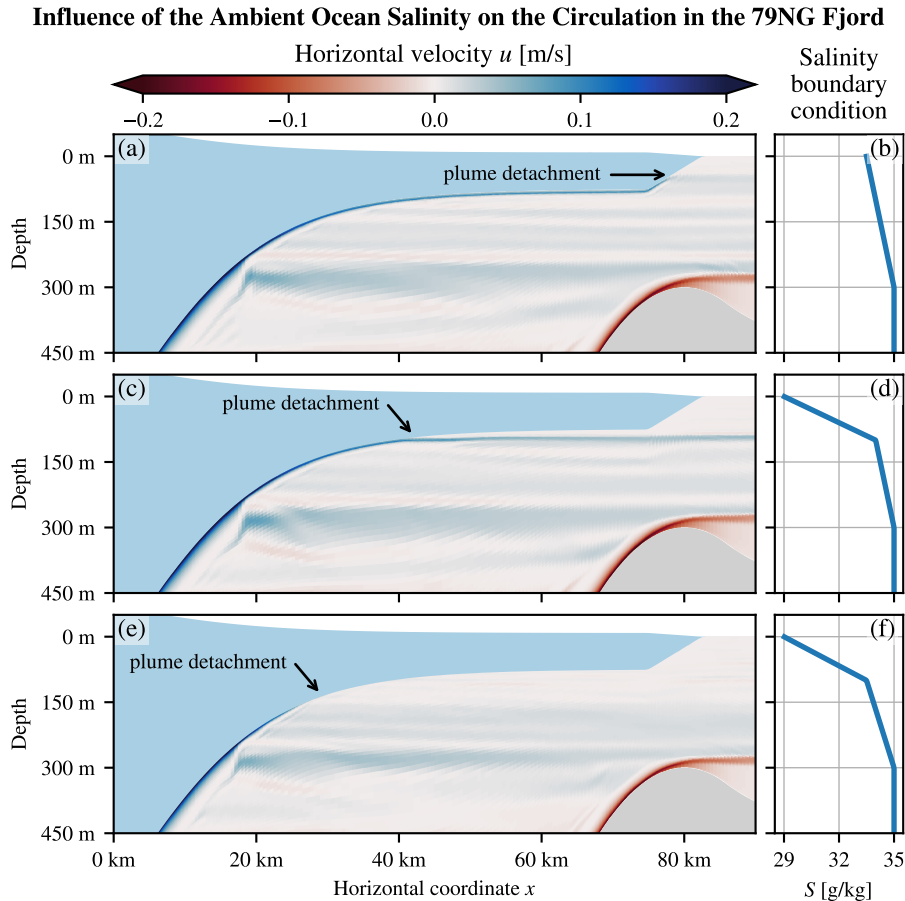


Figure 7. Experiments on the sensitivity of 79NG to the open ocean stratification, with higher salinity (a,b) than in our default scenario (c,d) as well as lower salinity (e,f). For higher salinities above the sill, the subglacial plume propagates further along the ice tongue and detaches higher up. The salinity at the level of plume detachment is always around 33.7 g kg^{-1} . When the plume detaches early (e), a weaker secondary plume develops above.

604 In fact, it is the salinity of the open ocean that determines the depth where the plume
 605 detaches. The salinity at the detachment level is $(33.7 \pm 0.1) \text{ g kg}^{-1}$ in all three scenar-
 606 ios. We also tested a stratification with a minimum salinity of 34 g kg^{-1} (not shown),
 607 in which case the plume never detaches from the ice tongue but reaches sea level. The
 608 reason that the detachment depth depends strongly on salinity is that at this level, the

609 plume density equals that of the ambient ocean, which is set primarily by salinity in the
610 79NG fjord.

611 For the deeper half of the ice tongue, the plume developments and meltrates are
612 basically identical between our sensitivity experiments, but they differ in the upper 300 m.
613 At the plume detachments, the subglacial meltrates drop to almost zero, which shows
614 again that the subglacial plume is responsible for the bulk of basal melting. In the scenario
615 with the plume detachment at great depths, a small second plume develops above
616 the main detachment, causing some more melting with meltrates up to 0.7 m yr^{-1} be-
617 fore detaching near 100 m depth (Fig. 7e). Only in the scenario with a late plume de-
618 tachment, we observe meltrates above 0.2 m yr^{-1} along the whole ice tongue up to the
619 calving front. However, note that the plume development as it propagates up the calv-
620 ing front in this scenario (Fig. 7a) is not entirely realistic, because the calving front is
621 sloping in our model and not vertical (Section 2.2.1).

622 *3.3.2 Influence of the ambient ocean temperature*

623 We investigate the influence of the imposed temperature stratification at the open
624 ocean boundary by varying the temperatures of Polar Water (PW) and Atlantic Inter-
625 mediate Water (AIW) individually as well as together. In our model, PW occupies the
626 upper 100 m of the water column and has in the default scenario a linear temperature
627 profile with -1.5°C at sea level and -1.0°C at 100 m depth (Fig. 2b). AIW fills the wa-
628 ter column below 300 m depth and has a vertically homogeneous temperature of 1.5°C
629 by default. In between 100 m and 300 m, we apply a linear temperature gradient. In our
630 sensitivity study, we increase the temperatures of AIW and/or PW by 0.5 K or 1.0 K.
631 We also decrease AIW temperatures by 0.5 K and 1.0 K. Note that we cannot make PW
632 colder, because the surface temperature is just above freezing in our default scenario (Fig. 2b).

633 We observe that the AIW temperature has a clearly larger impact on the glacier
634 cavity than variations of PW temperature. With increasing AIW temperature, the sub-
635 glacial meltrate increases along the whole ice tongue (Table 2) and the point at which
636 the plume detaches moves upward. For AIW temperatures of 0.5°C , the plume detaches
637 below 130 m, for 2.5°C above 90 m depth. This can be explained by the increased tem-
638 perature forcing, which causes more melting and thereby a lighter plume that rises faster
639 and further. Interestingly, in the deep part of the cavity, the thickness of the subglacial
640 plume is not much altered by temperature differences, although this is the part where
641 AIW is present.

642 The effects associated with increased PW temperatures are much smaller. Cavity
643 circulation and both plumes look practically the same as in the default scenario. The
644 only (small) difference we observe is in the detachment point of the subglacial plume.
645 It moves about 2 m down for a PW temperature increase of 0.5 K and about 3 m (com-
646 pared to default) for a 1.0 K-increase. This makes sense because the upper part of the
647 water column is lighter for warmer PW, so the plume reaches its neutral buoyancy ear-
648 lier. Since subglacial melting almost stops when the plume detaches, the overall meltrate
649 is slightly lower for higher PW temperatures (Table 2). However, note that our model
650 does not simulate calving, which can be intensified in warmer water.

651 When we increase the temperatures of both AIW and PW together, thus making
652 the whole water column warmer, we observe a combination of the effects described above.
653 The results look similar to those with only increased AIW temperatures, but the sub-
654 glacial plume detaches at a slightly deeper level.

655 *3.3.3 Role of the subglacial discharge*

656 The meltwater discharged at the grounding line has an important influence on sub-
657 glacial melt. In our default scenario, we prescribe a constant subglacial discharge of $70 \text{ m}^3 \text{ s}^{-1}$,

658 which is the value reported by a field campaign (Schaffer et al., 2020), and we find a clear,
 659 peaked meltrate maximum just after the grounding line. In contrast, if we reduce the
 660 discharged water volume in our model by an order of magnitude to $7 \text{ m}^3 \text{ s}^{-1}$, we observe
 661 a flatter melt distribution after the grounding line with a lower and rather constant meltrate
 662 over the first 10 km (Fig. 3e). Interestingly, after the splitting of the subglacial plume,
 663 the melt distributions look similar for low discharge and normal discharge (Fig. 3e). Also,
 664 the position of the plume detachment from the ice tongue is not much different. These
 665 observations suggest that the subglacial discharge has mostly an impact on the early de-
 666 velopment of the plume, while further away from the grounding line, the plume devel-
 667 opment is mostly determined by subglacial melting and the ambient ocean stratification.

668 Due to the decreased subglacial melting in scenarios with lower subglacial discharge,
 669 the cavity water is warmer, saltier, and denser. This has the effect that the dense bot-
 670 tom plume does not propagate as far down the slope and detaches earlier from the bot-
 671 tom. Also, both plumes are thinner and slower than in the default scenario. The strength
 672 of the overturning circulation is reduced by about one third to 26 mSv for a discharge
 673 of $7 \text{ m}^3 \text{ s}^{-1}$ (Table 2).

674 We observe the opposite effects when we increase the subglacial discharge: The meltrate
 675 increases; the cavity water becomes colder, fresher, and lighter; the plumes are thicker
 676 and faster. Doubling the discharge to $140 \text{ m}^3 \text{ s}^{-1}$ increases the overturning strength by
 677 about one fourth (relative to default scenario) to 50 mSv and the average meltrate by
 678 about one sixth to 14.3 myr^{-1} (Table 2).

679 In our model, we cannot reasonably increase the subglacial discharge arbitrarily.
 680 For example, with a discharge of $700 \text{ m}^3 \text{ s}^{-1}$ (ten-times the default), the large amount
 681 of meltwater leaving the cavity cannot be transported across the open boundary, because
 682 the prescribed conditions at the open boundary correspond to the default scenario, which
 683 has lower discharge and melting. This causes a density front near the open boundary,
 684 which is physically unstable and prevents the system from reaching a steady state. Nev-
 685 ertheless, the model stays numerically stable, even in such a non-equilibrium situation.

686 3.3.4 Role of the sill

687 Our model allows us to test a hypothesis made by Schaffer et al. (2020) based on
 688 their hydrographic measurements. They claim that the bathymetry of the 79NG fjord
 689 constrains the heat transport from the open Atlantic ocean into the glacier cavity. Ac-
 690 cording to Schaffer et al. (2020), the height of the sill at the fjord entrance determines
 691 how much warm AIW flows into the fjord, and in turn how much heat is available for
 692 subglacial melting. In our idealized 2D model, we can easily modify the sill height (de-
 693 fault: 300 m below sea level) or remove the sill completely and check which impact it has.

694 We find that the cavity water is clearly colder with a higher sill than with a lower
 695 sill or without a sill (Fig. 8a,b, see also Fig. 3c). The higher the sill, the stronger the tem-
 696 perature contrast between the water in the cavity and the water on the continental shelf.
 697 Consequently, the meltrate is larger if the sill is at greater depths and *vice versa* (Fig. 8c,d).
 698 Interestingly, the meltrate is not larger over the full length of the ice tongue, but mostly
 699 in the $(20 \pm 5) \text{ km}$ after the grounding line, where the ice is at great depths. The melt-
 700 ing of the thinner part of the ice tongue is not much influenced by the sill, neither is the
 701 position of the plume detachment from the ice. When the sill is at 350 m below sea level
 702 or deeper, the meltrate is almost independent of the sill depth (Fig. 8c,d). At this depth,
 703 the sill cannot effectively prevent the warm AIW from entering the cavity anymore.

704 So our simulations show that indeed the sill height constrains the heat transport
 705 into the cavity and thereby determines the meltrate of the 79NG ice tongue. This “sill
 706 effect” almost ends at a depth of about 350 m, measured from sea level.

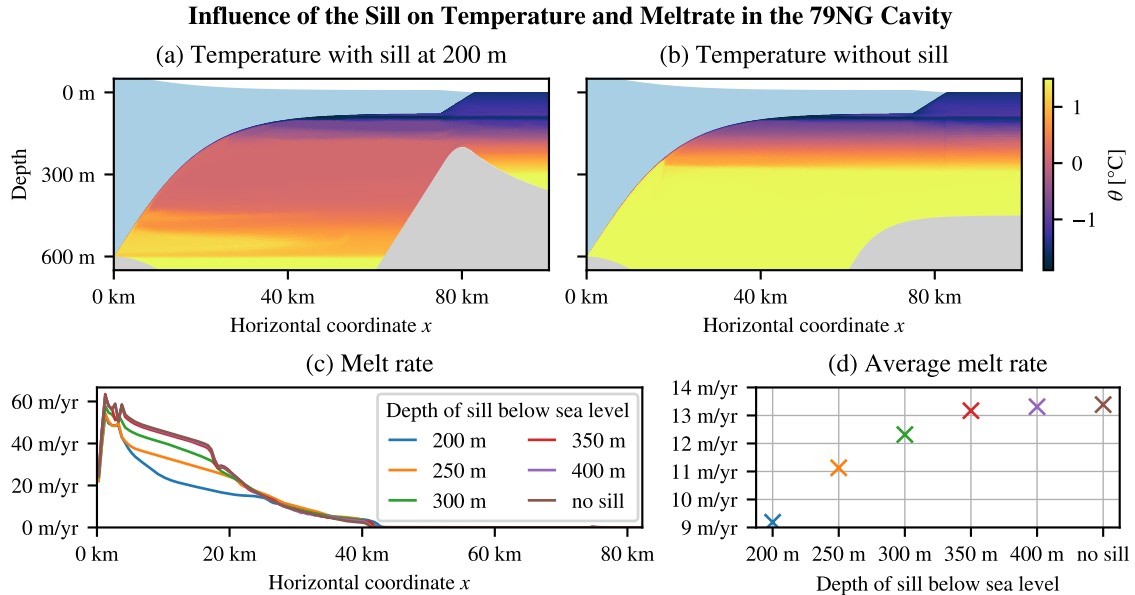


Figure 8. Temperature in the glacier cavity in a modified 79NG fjord with a high sill (a) and with no sill (b), as well as subglacial meltrate of the 79NG ice tongue with x -resolution (c) and in spatial average (d) for different sill depths (including no sill). When the sill is higher, *i.e.*, with a lower sill depth, less warm water can flow into the cavity, so the meltrate is lower. Note that the continental shelf offshore the cavity is at 450 m below sea level, so a sill depth of 450 m means no sill.

707

3.3.5 Roughness length

708

709

710

711

712

713

714

In our setup, the smoothness or roughness of the ice tongue on its underside is modeled by a roughness length, $z_{0,ice}$. This parameter has the value 0.01 m in our default scenario, but it is poorly known which value is realistic for a given ice shelf (P. R. Holland & Feltham, 2006). To test the sensitivity of the 79NG system on this value, we increased the roughness length by a factor of ten ($z_{0,ice} = 0.1$ m, scenario z0p) and decreased it by a factor of ten ($z_{0,ice} = 0.001$ m, scenario z0m). We also tested intermediate values to ensure that our observations are actually tendencies as reported below.

715

716

717

718

719

720

721

Our model results show that the shorter the roughness length, the larger the meltrate and the stronger the overturning circulation (Table 2). Due to the higher melting, the subglacial plume becomes colder (Fig. 9c,d), fresher, and more buoyant. It accelerates faster and has a higher velocity under the ice and after its detachment (Fig. 9a,b). Also the dense bottom plume is faster with a shorter roughness length (not shown). Even though the subglacial plume is fresher, the parameterized melt layer at the ice–ocean interface (Section 2.2.3) is actually saltier for smoother ice.

722

723

724

725

726

727

728

729

In the scenario z0p, most of the plume detaches from the ice tongue already at a depth of 200 m and leaves the fjord at this level, while the outflow at 100 m-depth is much weaker (Fig. 9b,d). Initially, the plume thickens quickly but detrains strongly around 23 km from the grounding line, so after this point, the plume is thinner than in the other two scenarios. In the scenario z0m, the plume is everywhere thinner than in the default scenario. One reason is that the entrainment is reduced because it must overcome a stronger stratification between plume and cavity water. So the high buoyancy of the plume reduces the entrainment of ambient water and thereby reduces the plume thickening, as

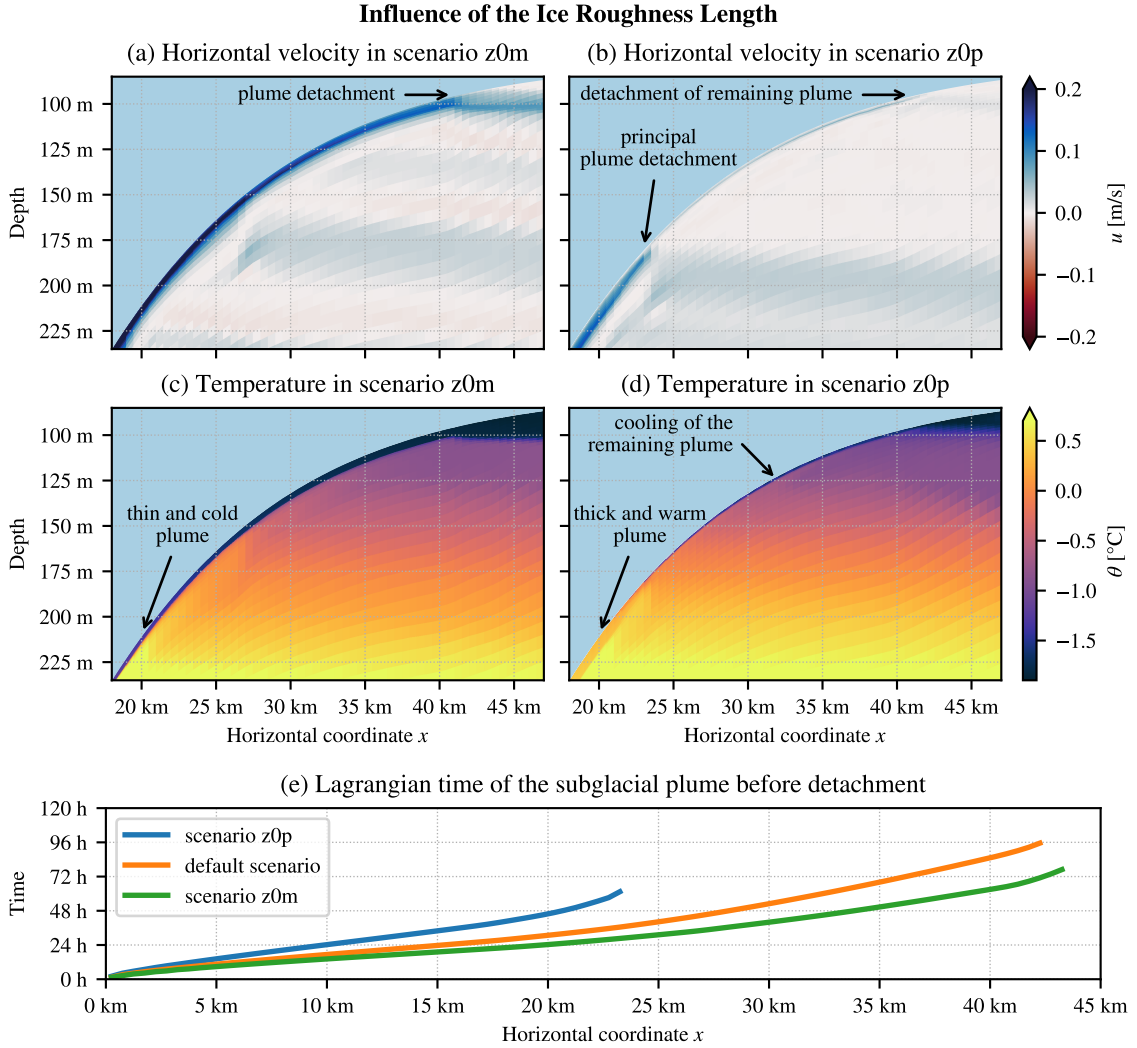


Figure 9. Influence of the roughness length of the ice tongue, $z_{0,ice}$, on the circulation (a,b) and the temperature (c,d) below the ice tongue as well as on the Lagrangian time of the subglacial plume (e). The Lagrangian time t , defined as the integral of $dt = dx/\bar{u}$, is shown up to the (principal) plume detachment, see panels (a), (b), and Fig. 3; this position is identified by a clear reduction of under-ice velocity u and plume velocity \bar{u} .

730 predicted by classical two-layer entrainment theory. Another reason is that the stronger
 731 acceleration of the plume leads to a divergence, which also thins the plume.

732 Our findings are consistent with the study of a subglacial plume by Burchard et
 733 al. (2022), who analyzed the same scenarios in a 1D model. They also observed thicker
 734 plumes for longer roughness lengths and less entrainment for shorter roughness lengths.
 735 Regarding subglacial melting, Burchard et al. (2022) observed at the beginning of the
 736 plume development higher melt rates in the scenarios with smoother ice. After about one
 737 week, the relation is reversed and the melt rate increases with the ice roughness, as pre-
 738 dicted by equilibrium theory. However, our 2D model suggests that the subglacial plume
 739 in the 79NG fjord does not actually reach this equilibrium state. The plumes in all ana-
 740 lyzed scenarios need – in a Lagrangian sense – less than four days to reach the point
 741 at which they detach from the ice tongue (Fig. 9e). Thus, our results correspond to the

742 initial plume development in the study of Burchard et al. (2022), where meltrates are
 743 higher for smoother ice.

744 4 Discussion

745 In large-scale ocean models without explicitly resolved glacier cavities, meltwater
 746 from fjords is often introduced at the sea surface (e.g., Stolzenberger et al., 2022). Our
 747 model results show that this is generally not realistic. In fact, the bulk of meltwater leaves
 748 the 79NG fjord in our default scenario between 90 m and 100 m below sea level (Section 3.1
 749 and Fig. 3a–c). This level depends primarily on the stratification of the ambient ocean,
 750 which is mainly set by salinity. Even a relatively small change in the upper ocean salin-
 751 ity can alter the outflow depth of glacially modified water by 50 m (Section 3.3.1 and Fig. 7).
 752 The temperature stratification also influences the outflow depth, but less dramatically,
 753 as our sensitivity study shows (Section 3.3.2). On the other hand, the outflow depth is
 754 almost unaffected by the subglacial discharge and by the sill at the fjord entrance, de-
 755 spite their big influence on subglacial melting and overturning circulation in the cavity
 756 (Sections 3.3.3 and 3.3.4). If the base of the ice tongue had a higher roughness, the out-
 757 flow around 95 m depth would be weaker but still at the same depth as for smooth ice
 758 (Section 3.3.5 and Fig. 9a,b). We suspect that the outflow depth of meltwater does not
 759 change much with seasons, because the fjord properties that have a strong seasonality
 760 are the subglacial runoff (Lindeman et al., 2020; Schaffer et al., 2020) and the ocean sur-
 761 face temperature, which both have little impact on the outflow level. Whether the sub-
 762 surface stratification at 79NG, which is important for the outflow depth, shows seasonal
 763 variability, is still unknown, but the existing mooring data shows no clear signature of
 764 a seasonal cycle (Lindeman et al., 2020; Schaffer et al., 2020, and own analysis of their
 765 datasets). Longer time series of measurements at 79NG are necessary to answer this ques-
 766 tion.

767 The depth at which meltwater leaves the glacier fjord is not only relevant for the
 768 export of glacially modified water but also for the development of the ice tongue. Our
 769 simulations show that most subglacial melting occurs while the subglacial plume is at
 770 the ice–ocean interface. When the plume detaches, the meltrate drops to almost zero.
 771 This happens roughly at the same level as the meltwater outflow. Thus, oceanographic
 772 measurements of the depth of glacially modified water near a glacier fjord can be used
 773 to infer which part of the glacier tongue is likely to show high basal meltrates. This in-
 774 formation can be helpful for a decision of where to install measurement stations on a float-
 775 ing ice tongue to monitor ice thickness changes.

776 At the depth where the subglacial plume propagates away from the ice tongue, the
 777 vertical coordinate levels in our model accumulate. This ensures that the water prop-
 778 erties of the plume are preserved over long distances with little spurious mixing. It is achieved
 779 automatically by the stratification zooming of AVC. No *a priori* knowledge of the po-
 780 sition of plume detachment is needed, which is an important difference to non-adaptive
 781 coordinates that can achieve high vertical resolutions in pre-defined regions. Moreover,
 782 AVC change the vertical layer distribution with time, for example in simulations with
 783 tides or other time-varying forcings that alter the stratification.

784 With z -coordinates, which are often used to model the ocean under an ice tongue
 785 or an ice shelf (e.g., Losch, 2008), it would be difficult to obtain equally detailed sim-
 786 ulations of the cavity circulation and in particular of the subglacial plume. Due to their
 787 step-wise manner of resolving the ice–ocean interface, z -coordinates are usually too dif-
 788 fusive to preserve the plume over longer distances. Without a well-preserved plume, an
 789 analysis of the entrainment rate as shown in Fig. 6 would not be feasible. An insufficient
 790 representation of the plume development has also implications on the accuracy of the
 791 computation of basal meltrates (Burchard et al., 2022). Furthermore, a good simulation

of meltwater export from the fjord into the open ocean demands a good preservation of the plume properties with minimal spurious mixing. This can be provided by AVC.

While AVC (Hofmeister et al., 2010) have a number of characteristics, the main feature used in our setup is their capability to zoom towards stratification. This enables high resolutions in the entrainment layers of both plumes and allows the coordinates to follow the outflow to a reasonable extent, so that glacially modified water can be transported far offshore. This stratification zooming could be combined with other modeling approaches like vertical Lagrangian remapping or the Arbitrary Lagrangian-Eulerian (ALE) method. In these methods, Lagrangian motion of the model grid is followed by a regrid step, in which the coordinate surfaces are moved back to prescribed target positions; the physical fields are then mapped onto this new grid in a remap step (Griffies et al., 2020). The target coordinate layout could be prescribed based on the ocean stratification in the current model state. Such an approach would combine the advantages of ALE with the advantages of stratification zooming shown in this paper.

As for terrain-following coordinates in general, the calving front presents a challenge for AVC. Our setup uses a gentle slope instead of an almost vertical wall at the ice front to make sure that the plume is well preserved as it leaves the cavity. This part of the ice tongue could possibly be simulated more realistically by a modification of the cost function that determines the zooming of AVC. Instead of zooming to stratification and the sea surface, it might be advantageous to zoom only to stratification and the ice-ocean interface but not to the atmosphere-ocean interface. This way, more layers could be available at the calving front to allow a high calving front slope as well as a good preservation of plume properties. Since AVC (Hofmeister et al., 2010) have not been developed with glacier tongues in mind, and this paper presents their first application to an ice cavity, such a possibility has not yet been implemented. It should however be kept in mind that processes at the calving front are strongly non-hydrostatic in nature and therefore cannot be sufficiently reproduced with classical ocean models anyway.

While our idealized 79NG fjord model shows qualitatively realistic dynamics and processes under the glacier tongue, its quantitative results should be taken with a grain of salt, as exemplified by our sensitivity study on the sill depth (Section 3.3.4). We observe that the meltrate of the ice tongue (Fig. 8) and the strength of the overturning circulation in the cavity (Table 2) are very sensitive to the depth of the sill at the fjord entrance, which is 300 m in our default setup. However, no single value can be entirely realistic, because in the real system, the sill is not at the same depth over the whole fjord width (Fig. 1a). The depth of the sill, which is the shallowest point that inflowing water must cross, depends on the path from the open ocean into the cavity. It can be as deep as 325 m below sea level but also shallower (see Fig. 1 and Schaffer et al., 2020). Since this cross-fjord variability cannot be reproduced in 2D, the quantitative results of a 2D model can only be approximations.

5 Conclusions and Outlook

We developed a numerical ocean model of a glacier fjord in 2D with high horizontal and vertical resolution. The fjord and its forcing were built to resemble 79NG in an idealized, analytical way (Fig. 1 and 2). Quantitative results of our default simulation are a good approximation of reality. In particular, the subglacial meltrate and the strength of the overturning circulation are consistent between our model and measurements at the glacier (Table 2). Thanks to the simplicity of the model, its qualitative results (Fig. 3), which we explored further in a sensitivity study, will also hold for other glacier cavities.

Our model shows that the buoyant plume, which develops on the underside of the ice tongue, is responsible for the bulk of subglacial melting. When the plume reaches neutral buoyancy and detaches from the ice, basal melting almost stops. At this level, which

842 is about 95 m below sea level in our present-day (default) scenario, the plume transports
 843 meltwater out of the fjord towards the open ocean. The detachment depth is set primar-
 844 ily by the stratification of the ambient ocean, particularly its salinity (Fig. 7).

845 Furthermore, we confirmed that the depth of the sill at the fjord entrance has a
 846 big influence on the melt rate and the overturning strength in the fjord. With a deeper
 847 sill, the dense bottom plume brings more warm Atlantic water into the cavity and thus
 848 more heat is transported towards the ice tongue (Schaffer et al., 2020), which intensi-
 849 fies subglacial melting. In case of 79NG, this sill effect ends at around 350 m depth (Fig. 8).

850 The two plumes that make up the estuarine circulation in the glacier cavity are re-
 851 solved by our model in great detail (Fig. 4 and 6), thanks to the stratification-zooming
 852 of AVC (Hofmeister et al., 2010). We showed for the first time that with this modeling
 853 approach, a vertical resolution of less than 1 m in the entrainment layer of the buoyant
 854 plume under an ice tongue can be achieved (Fig. 4), which is important for the correct
 855 representation of subglacial melting and plume development (Burchard et al., 2022). The
 856 computational cost compared to non-adaptive σ -coordinates is increased by less than 10 %
 857 (Section 2.3), which is much cheaper than increasing the number of vertical layers. Fur-
 858 ther advantages of AVC are that they minimize the pressure gradient error (Hofmeister
 859 et al., 2010; Gräwe et al., 2015) and that they follow the plumes to some extent, which
 860 preserves the properties of the outflowing water mass well (Fig. 3). We believe that the
 861 application of AVC in more ocean models will mean an improvement to the way processes
 862 under ice tongues and ice shelves are simulated. When stratification zooming is used to-
 863 gether with a melt parametrization that is suitable for high vertical resolutions (Burchard
 864 et al., 2022), this can refine projections of ice sheet melting and glacier stability.

865 Given the successful demonstration of AVC in an idealized 2D glacier cavity, a next
 866 step should be to extend this setup into a realistic 3D model of the 79NG fjord. This
 867 should include resolving the across-fjord dimension with the same high resolution as the
 868 along-fjord direction, using the real geometry and topography of the fjord, as well as forc-
 869 ing the regional ocean model with actual observational or reanalysis data. Such a setup
 870 will allow to study effects that have been neglected so far, *e.g.*, the Coriolis effect, and
 871 will back up our qualitative results with accurate quantitative assessments.

872 **Appendix A Analytical description of the setup**

873 Our setup is built to resemble the 79NG fjord in an idealized way that can be com-
 874 pletely described by simple, analytical functions. Here we give the mathematical expres-
 875 sions of these functions for the future use of our setup as a reference test case.

876 **A1 Model bathymetry**

877 The definition of the default model bathymetry is based on the following points:

- 878 (P1) grounding line ($x = 0$) at $z_{\text{gline}} = -600$ m,
- 879 (P2) deepest point in the trough at $(x_{\text{trough}}, z_{\text{trough}}) = (41 \text{ km}, -900 \text{ m})$,
- 880 (P3) highest point of the sill at $(x_{\text{sill}}, z_{\text{sill}}) = (80 \text{ km}, -300 \text{ m})$,
- 881 (P4) continental shelf far offshore ($x \rightarrow \infty$) at $z_{\text{shelf}} = -450$ m,

882 together with the following conditions on the bottom slope dz/dx :

- 883 (S1) The slope is zero at the grounding line: $dz/dx = 0$ for $x = 0$.
- 884 (S2) The slope is at most 2.5 % in absolute value: $|dz/dx| \leq s_{\text{max}} = 0.025$ for all $x \in$
 885 $[0 \text{ km}, 150 \text{ km}]$.
- 886 (S3) The slope is a continuous function.

887 The last condition ensures that the bathymetry $z(x)$ is smooth, the other six conditions
 888 are derived from bathymetric measurements (Mayer et al., 2000; Schaffer et al., 2020),
 889 see Fig. 1. The combination of these seven conditions fully defines the glacier cavity as
 890 the concatenation of a third-order polynomial for the grounding line and the trough, a
 891 second-order polynomial for the sill, and a first-order polynomial in between, as explained
 892 in the following. With a choice of the transition point from sill to continental shelf (given
 893 below), also the exponentially decreasing shelf is fixed.

894 Conditions (P1,P2,S1) imply that the third-order polynomial going from the ground-
 895 ing line through the trough is

$$896 \quad z(x) = a_{\text{trough}}x^3 + b_{\text{trough}}x^2 + z_{\text{gline}}, \text{ with} \quad (\text{A1})$$

$$897 \quad b_{\text{trough}} = 3 \frac{z_{\text{trough}} - z_{\text{gline}}}{(x_{\text{trough}})^2}, \text{ and} \quad (\text{A2})$$

$$898 \quad a_{\text{trough}} = -\frac{2}{3} \frac{b_{\text{trough}}}{x_{\text{trough}}}. \quad (\text{A3})$$

899 In consequence of (S2), the trough ends at x_0 such that

$$900 \quad \frac{dz}{dx}(x_0) = 3a_{\text{trough}}x_0^2 + 2b_{\text{trough}}x_0 = s_{\text{max}}, \text{ where} \quad (\text{A4})$$

$$901 \quad z_0 = z(x_0) = a_{\text{trough}}x_0^3 + b_{\text{trough}}x_0^2 + z_{\text{gline}}. \quad (\text{A5})$$

902 From this point onward, the bathymetry is described by an (affine) linear function with
 903 slope s_{max} (S2,S3):

$$904 \quad z(x) = z_0 + s_{\text{max}}(x - x_0). \quad (\text{A6})$$

905 The upper end point of this slope, (x_1, z_1) , must be chosen such that (S3) is fulfilled for
 906 the parabolic sill defined by (P3) and starting at (x_1, z_1) :

$$907 \quad z(x) = \frac{a_{\text{sill}}}{2}(x - x_{\text{sill}})^2 + z_{\text{sill}}, \text{ with} \quad (\text{A7})$$

$$908 \quad a_{\text{sill}} = \frac{s_{\text{max}}}{x_1 - x_{\text{sill}}}. \quad (\text{A8})$$

909 As eastern end point of the parabola, (x_2, z_2) , we choose the position where its slope equals
 910 $-s_{\text{max}}/2$. At this point, an exponential function with the same slope starts (S3) and de-
 911 creases in accordance with (P4):

$$912 \quad z(x) = a_{\text{shelf}} \exp(b_{\text{shelf}}x) + z_{\text{shelf}}, \text{ with} \quad (\text{A9})$$

$$913 \quad a_{\text{shelf}} = \frac{z_2 - z_{\text{shelf}}}{\exp(b_{\text{shelf}}x_2)}, \text{ and} \quad (\text{A10})$$

$$914 \quad b_{\text{shelf}} = a_{\text{sill}} \frac{x_2 - x_{\text{sill}}}{z_2 - z_{\text{shelf}}}. \quad (\text{A11})$$

915 In the sensitivity experiment with the sill at $z_{\text{sill}} = -400$ m (Section 3.3.4), we
 916 put the connection between parabolic sill and exponential shelf at the point where the
 917 bottom slope equals $-s_{\text{max}}/3$, to avoid $z_2 < z_{\text{shelf}}$. In the scenario without a sill, the
 918 linear slope connects directly to an exponentially increasing shelf at $z_1 = -600$ m.

919 A Python implementation of the here-explained mathematical expressions is pro-
 920 vided with the model setup (Reinert, 2023b) that belongs to this paper.

921 **A2 Model ice topography**

922 The position of the lower ice edge is defined in our model in two parts. Between
 923 the grounding line and the calving front, we use a hyperbolic tangent shape:

$$924 \quad \eta(x) = a_{\text{ice}} \tanh[b_{\text{ice}}(x - c_{\text{ice}})] + d_{\text{ice}}. \quad (\text{A12})$$

925 A reasonable choice of the parameters and a good fit to the ice shape near the ground-
 926 ing line (Fig. 1b) is obtained if the maximum ice slope is at the grounding line ($x = 0$)
 927 and has a value of $\max(d\eta/dx) = s_{\max} = 0.025$. This greatly simplifies the expres-
 928 sion, since $c_{\text{ice}} = 0$, thus $d_{\text{ice}} = z_{\text{gline}}$, and $b_{\text{ice}} = s_{\max}/a_{\text{ice}}$. We further take $a_{\text{ice}} =$
 929 525 m, so that the ice topography converges to $\eta = -75$ m (Fig. 1b). The Python code
 930 for the model setup (Reinert, 2023b) provided with this paper also implements the op-
 931 tion of a maximum slope at a position c_{ice} different from the grounding line (not used
 932 in this paper), but this requires computing a_{ice} numerically to fulfill the condition that
 933 η converges to -75 m in eastward direction.

934 After the calving front ($x = 75$ km), we linearly connect the lower ice edge with
 935 sea level. The linear connection has a slope of 1%, which ensures a low perturbation of
 936 the subglacial plume as it passes under the calving front (Fig. 3). With a modification
 937 of the vertical coordinates as discussed in Section 4, a higher slope might be feasible.

938 A3 Model stratification

939 Our model uses as initial and boundary conditions the same horizontally homo-
 940 geneous stratification. The stratification is defined by specifying temperature and salin-
 941 ity at three vertical positions, with a linear interpolation of the values in between and
 942 a constant extrapolation below. In our default scenario, the salinity-values are $S(z =$
 943 $0) = 29 \text{ g kg}^{-1}$, $S(z = -100 \text{ m}) = 34 \text{ g kg}^{-1}$, $S(z = -300 \text{ m}) = 35 \text{ g kg}^{-1}$ (Fig. 2a).
 944 The temperature-values are $\theta(z = 0) = -1.5 \text{ }^\circ\text{C}$, $\theta(z = -100 \text{ m}) = -1.0 \text{ }^\circ\text{C}$, $\theta(z =$
 945 $-300 \text{ m}) = 1.5 \text{ }^\circ\text{C}$ (Fig. 2b). The modified values in the sensitivity study are given in
 946 Sections 3.3.1 and 3.3.2.

947 Open Research

948 The model setup can be downloaded from <https://doi.org/10.5281/zenodo.7755753>
 949 (Reinert, 2023b) together with instructions how to reproduce the simulations presented
 950 in this paper. The corresponding GETM source code can be downloaded from <https://doi.org/10.5281/zenodo.7741925> (Klingbeil, 2023). The model output generated by
 951 this code and presented in this manuscript can be downloaded from <https://doi.org/10.5281/zenodo.7755908> (Reinert, 2023a).

954 This paper contains no unpublished observational data. Figure 1 uses bathymetry
 955 data published by Mayer et al. (2000) and Schaffer et al. (2019). Figure 2 shows CTD
 956 profile 115-1 from *Polarstern* cruise PS109 published by Kanzow et al. (2018).

957 Acknowledgments

958 The work of this study has been supported by the collaborative research project GROCE
 959 (Greenland Ice Sheet–Ocean Interaction) funded by the German Federal Ministry of Ed-
 960 ucation and Research (BMBF, grant 03F0855E). This paper is a contribution to the projects
 961 M5 (Reducing Spurious Mixing and Energetic Inconsistencies in Realistic Ocean-Modelling
 962 Applications) and S1 (Diagnosis and Metrics in Climate Models) of the collaborative re-
 963 search center TRR 181 “Energy Transfers in Atmosphere and Ocean” funded by the Ger-
 964 man Research Foundation (DFG, project 274762653). ML is supported by ECAS-BALTIC
 965 funded by the German Federal Ministry of Education and Research (BMBF, grant 03F0860H).
 966 We thank Sarah Vierling (Amherst College, Massachusetts, USA) for extending the code
 967 used to create the model setup and for running many sensitivity experiments during an
 968 internship supervised by Markus Reinert in Hans Burchard’s lab, funded by the German
 969 Academic Exchange Service (DAAD) in the program “RISE Germany”. Figures in this
 970 paper use the colormaps of the cmocean package (Thyng et al., 2016).

References

971
972
973
974
975
976
977
978
979
980
981
982
983
984
985
986
987
988
989
990
991
992
993
994
995
996
997
998
999
1000
1001
1002
1003
1004
1005
1006
1007
1008
1009
1010
1011
1012
1013
1014
1015
1016
1017
1018
1019
1020
1021
1022
1023
1024
1025

- Arneborg, L., Fiekas, V., Umlauf, L., & Burchard, H. (2007). Gravity Current Dynamics and Entrainment—A Process Study Based on Observations in the Arkona Basin. *Journal of Physical Oceanography*, *37*(8), 2094–2113. doi: 10.1175/JPO3110.1
- Aschwanden, A., Fahnestock, M. A., Truffer, M., Brinkerhoff, D. J., Hock, R., Khroulev, C., ... Khan, S. A. (2019). Contribution of the Greenland Ice Sheet to sea level over the next millennium. *Science Advances*, *5*(6), eaav9396. doi: 10.1126/sciadv.aav9396
- Burchard, H., & Beckers, J.-M. (2004). Non-uniform adaptive vertical grids in one-dimensional numerical ocean models. *Ocean Modelling*, *6*(1), 51–81. doi: 10.1016/S1463-5003(02)00060-4
- Burchard, H., & Bolding, K. (2002). *GETM – A General Estuarine Transport Model* (Tech. Rep. No. EUR 20253 EN). European Commission.
- Burchard, H., Bolding, K., Jenkins, A., Losch, M., Reinert, M., & Umlauf, L. (2022). The Vertical Structure and Entrainment of Subglacial Melt Water Plumes. *Journal of Advances in Modeling Earth Systems*, *14*(3), e2021MS002925. doi: 10.1029/2021MS002925
- Burchard, H., Bolding, K., & Villarreal, M. R. (1999). *GOTM, a general ocean turbulence model: Theory, implementation and test cases*. Space Applications Institute.
- Burchard, H., & Petersen, O. (1997). Hybridization between sigma- and z-coordinates for improving the internal pressure gradient calculation in marine models with steep bottom slopes. *International Journal for Numerical Methods in Fluids*, *25*(9), 1003–1023. doi: 10.1002/(SICI)1097-0363(19971115)25:9<1003::AID-FLD600>3.0.CO;2-E
- Chegini, F., Holtermann, P., Kerimoglu, O., Becker, M., Kreuz, M., Klingbeil, K., ... Burchard, H. (2020). Processes of Stratification and Destratification During An Extreme River Discharge Event in the German Bight ROFI. *Journal of Geophysical Research: Oceans*, *125*(8), e2019JC015987. doi: 10.1029/2019JC015987
- Christmann, J., Helm, V., Khan, S. A., Kleiner, T., Müller, R., Morlighem, M., ... Humbert, A. (2021). Elastic deformation plays a non-negligible role in Greenland’s outlet glacier flow. *Commun Earth Environ*, *2*(1), 1–12. doi: 10.1038/s43247-021-00296-3
- Goldberg, D., Holland, D. M., & Schoof, C. (2009). Grounding line movement and ice shelf buttressing in marine ice sheets. *Journal of Geophysical Research: Earth Surface*, *114*(F4). doi: 10.1029/2008JF001227
- Gräwe, U., Holtermann, P., Klingbeil, K., & Burchard, H. (2015). Advantages of vertically adaptive coordinates in numerical models of stratified shelf seas. *Ocean Modelling*, *92*, 56–68. doi: 10.1016/j.ocemod.2015.05.008
- Griffies, S. M., Adcroft, A., & Hallberg, R. W. (2020). A Primer on the Vertical Lagrangian-Remap Method in Ocean Models Based on Finite Volume Generalized Vertical Coordinates. *Journal of Advances in Modeling Earth Systems*, *12*(10), e2019MS001954. doi: 10.1029/2019MS001954
- Gwyther, D. E., Kusahara, K., Asay-Davis, X. S., Dinniman, M. S., & Galton-Fenzi, B. K. (2020). Vertical processes and resolution impact ice shelf basal melting: A multi-model study. *Ocean Modelling*, *147*, 101569. doi: 10.1016/j.ocemod.2020.101569
- Haney, R. L. (1991). On the Pressure Gradient Force over Steep Topography in Sigma Coordinate Ocean Models. *Journal of Physical Oceanography*, *21*(4), 610–619. doi: 10.1175/1520-0485(1991)021<0610:OTPGFO>2.0.CO;2
- Hofmeister, R., Burchard, H., & Beckers, J.-M. (2010). Non-uniform adaptive vertical grids for 3D numerical ocean models. *Ocean Modelling*, *33*(1), 70–86. doi: 10.1016/j.ocemod.2009.12.003

- 1026 Holland, D. M., & Jenkins, A. (1999). Modeling Thermodynamic Ice–Ocean Inter-
 1027 actions at the Base of an Ice Shelf. *J. Phys. Oceanogr.*, *29*(8), 1787–1800. doi:
 1028 10.1175/1520-0485(1999)029<1787:MTIOIA>2.0.CO;2
- 1029 Holland, P. R., & Feltham, D. L. (2006). The Effects of Rotation and Ice Shelf
 1030 Topography on Frazil-Laden Ice Shelf Water Plumes. *Journal of Physical*
 1031 *Oceanography*, *36*(12), 2312–2327. doi: 10.1175/JPO2970.1
- 1032 Horwath, M., Gutknecht, B. D., Cazenave, A., Palanisamy, H. K., Marti, F.,
 1033 Marzeion, B., ... Benveniste, J. (2022). Global sea-level budget and
 1034 ocean-mass budget, with a focus on advanced data products and uncer-
 1035 tainty characterisation. *Earth System Science Data*, *14*(2), 411–447. doi:
 1036 10.5194/essd-14-411-2022
- 1037 Huang, R. X. (1993). Real Freshwater Flux as a Natural Boundary Condition for
 1038 the Salinity Balance and Thermohaline Circulation Forced by Evaporation and
 1039 Precipitation. *Journal of Physical Oceanography*, *23*(11), 2428–2446. doi:
 1040 10.1175/1520-0485(1993)023<2428:RFFAAN>2.0.CO;2
- 1041 Humbert, A., Christmann, J., Corr, H. F. J., Helm, V., Höyns, L.-S., Hofstede, C.,
 1042 ... Zeising, O. (2022). On the evolution of an ice shelf melt channel at the
 1043 base of Filchner Ice Shelf, from observations and viscoelastic modeling. *The*
 1044 *Cryosphere*, *16*(10), 4107–4139. doi: 10.5194/tc-16-4107-2022
- 1045 Inall, M. E., & Gillibrand, P. A. (2010). The physics of mid-latitude fjords: A re-
 1046 view. *Geological Society, London, Special Publications*, *344*(1), 17–33. doi: 10
 1047 .1144/SP344.3
- 1048 IOC, SCOR, & IAPSO. (2010). The international thermodynamic equation of sea-
 1049 water – 2010: Calculation and use of thermodynamic properties. *Intergovern-*
 1050 *mental Oceanographic Commission, Manuals and Guides No. 56, UNESCO.*
 1051 doi: 10.25607/OBP-1338
- 1052 IPCC. (2022). Summary for policymakers [Book Section]. In H. O. Pörtner et al.
 1053 (Eds.), *Climate change 2022: Impacts, adaptation, and vulnerability. contribu-*
 1054 *tion of working group ii to the sixth assessment report of the intergovernmental*
 1055 *panel on climate change* (p. In Press). Cambridge, UK: Cambridge University
 1056 Press. (In Press)
- 1057 Jenkins, A., Hellmer, H. H., & Holland, D. M. (2001). The Role of Meltwater
 1058 Advection in the Formulation of Conservative Boundary Conditions at an
 1059 Ice–Ocean Interface. *Journal of Physical Oceanography*, *31*(1), 285–296. doi:
 1060 10.1175/1520-0485(2001)031<0285:TROMAI>2.0.CO;2
- 1061 Kanzow, T., Schaffer, J., & Rohardt, G. (2018). *Physical oceanography dur-*
 1062 *ing POLARSTERN cruise PS109 (ARK-XXXI/4).* PANGAEA. doi:
 1063 10.1594/PANGAEA.885358
- 1064 Kappelsberger, M. T., Strößenreuther, U., Scheinert, M., Horwath, M., Groh, A.,
 1065 Knöfel, C., ... Khan, S. A. (2021). Modeled and Observed Bedrock Dis-
 1066 placements in North-East Greenland Using Refined Estimates of Present-Day
 1067 Ice-Mass Changes and Densified GNSS Measurements. *Journal of Geophysical*
 1068 *Research: Earth Surface*, *126*(4), e2020JF005860. doi: 10.1029/2020JF005860
- 1069 Klingbeil, K. (2023). *Source code for the coastal ocean model GETM (glacial_ice*
 1070 *branch).* Zenodo. (Model code) doi: 10.5281/zenodo.7741925
- 1071 Klingbeil, K., & Burchard, H. (2013). Implementation of a direct nonhydrostatic
 1072 pressure gradient discretisation into a layered ocean model. *Ocean Modelling*,
 1073 *65*, 64–77. doi: 10.1016/j.ocemod.2013.02.002
- 1074 Klingbeil, K., Lemarié, F., Debreu, L., & Burchard, H. (2018). The numerics of hy-
 1075 drostatic structured-grid coastal ocean models: State of the art and future per-
 1076 spectives. *Ocean Modelling*, *125*, 80–105. doi: 10.1016/j.ocemod.2018.01.007
- 1077 Klingbeil, K., Mohammadi-Aragh, M., Gräwe, U., & Burchard, H. (2014).
 1078 Quantification of spurious dissipation and mixing – Discrete variance de-
 1079 cay in a Finite-Volume framework. *Ocean Modelling*, *81*, 49–64. doi:
 1080 10.1016/j.ocemod.2014.06.001

- 1081 Li, Q., Bruggeman, J., Burchard, H., Klingbeil, K., Umlauf, L., & Bolding, K.
 1082 (2021). Integrating CVMix into GOTM (v6.0): A consistent framework for
 1083 testing, comparing, and applying ocean mixing schemes. *Geoscientific Model*
 1084 *Development*, *14*(7), 4261–4282. doi: 10.5194/gmd-14-4261-2021
- 1085 Lindeman, M. R., Straneo, F., Wilson, N. J., Toole, J. M., Krishfield, R. A., Beaird,
 1086 N. L., . . . Schaffer, J. (2020). Ocean Circulation and Variability Beneath
 1087 Nioghalvfjærdsbræ (79 North Glacier) Ice Tongue. *Journal of Geophysical*
 1088 *Research: Oceans*, *125*(8), e2020JC016091. doi: 10.1029/2020JC016091
- 1089 Losch, M. (2008). Modeling ice shelf cavities in a z coordinate ocean general circulation
 1090 model. *Journal of Geophysical Research: Oceans*, *113*(C8). doi: 10.1029/
 1091 2007JC004368
- 1092 Mayer, C., Reeh, N., Jung-Rothenhäusler, F., Huybrechts, P., & Oerter, H. (2000).
 1093 The subglacial cavity and implied dynamics under Nioghalvfjærdsfjorden
 1094 Glacier, NE-Greenland. *Geophysical Research Letters*, *27*(15), 2289–2292.
 1095 doi: 10.1029/2000GL011514
- 1096 Mulwijk, M., Straneo, F., Slater, D. A., Smedsrud, L. H., Holte, J., Wood, M., . . .
 1097 Harden, B. (2022). Export of Ice Sheet Meltwater from Upernavik Fjord,
 1098 West Greenland. *Journal of Physical Oceanography*, *52*(3), 363–382. doi:
 1099 10.1175/JPO-D-21-0084.1
- 1100 Reinert, M. (2023a). *Output files of the 2DV-model for the 79NG fjord*. Zenodo.
 1101 (Dataset) doi: 10.5281/zenodo.7755908
- 1102 Reinert, M. (2023b). *Setup files of the 2DV-model for the 79NG fjord*. Zenodo.
 1103 (Model setup) doi: 10.5281/zenodo.7755753
- 1104 Rignot, E., & Steffen, K. (2008). Channelized bottom melting and stabil-
 1105 ity of floating ice shelves. *Geophysical Research Letters*, *35*(2). doi:
 1106 10.1029/2007GL031765
- 1107 Schaffer, J., Kanzow, T., von Appen, W.-J., von Albedyll, L., Arndt, J. E., &
 1108 Roberts, D. H. (2020). Bathymetry constrains ocean heat supply to Green-
 1109 land’s largest glacier tongue. *Nature Geoscience*, *13*(3), 227–231. doi:
 1110 10.1038/s41561-019-0529-x
- 1111 Schaffer, J., Timmermann, R., Arndt, J. E., Rosier, S. H. R., Anker, P. G. D.,
 1112 Callard, S. L., . . . Roberts, D. H. (2019). *An update to Greenland and Antarc-*
 1113 *tic ice sheet topography, cavity geometry, and global bathymetry (RTopo-2.0.4)*.
 1114 PANGAEA. doi: 10.1594/PANGAEA.905295
- 1115 Schaffer, J., von Appen, W.-J., Dodd, P. A., Hofstede, C., Mayer, C., de Steur, L.,
 1116 & Kanzow, T. (2017). Warm water pathways toward Nioghalvfjærdsfjorden
 1117 Glacier, Northeast Greenland. *Journal of Geophysical Research: Oceans*,
 1118 *122*(5), 4004–4020. doi: 10.1002/2016JC012462
- 1119 Shepherd, A., Wingham, D., & Rignot, E. (2004). Warm ocean is eroding
 1120 West Antarctic Ice Sheet. *Geophysical Research Letters*, *31*(23). doi:
 1121 10.1029/2004GL021106
- 1122 Stolzenberger, S., Rietbroek, R., Wekerle, C., Uebbing, B., & Kusche, J. (2022).
 1123 Simulated Signatures of Greenland Melting in the North Atlantic: A Model
 1124 Comparison With Argo Floats, Satellite Observations, and Ocean Reanaly-
 1125 sis. *Journal of Geophysical Research: Oceans*, *127*(11), e2022JC018528. doi:
 1126 10.1029/2022JC018528
- 1127 Straneo, F., & Cenedese, C. (2015). The Dynamics of Greenland’s Glacial Fjords
 1128 and Their Role in Climate. *Annu. Rev. Mar. Sci.*, *7*(1), 89–112. doi: 10.1146/
 1129 annurev-marine-010213-135133
- 1130 Thyng, K. M., Greene, C. A., Hetland, R. D., Zimmerle, H. M., & DiMarco, S. F.
 1131 (2016). True Colors of Oceanography: Guidelines for Effective and Accurate
 1132 Colormap Selection. *Oceanography*, *29*(3), 9–13.
- 1133 Timmermann, R., Wang, Q., & Hellmer, H. H. (2012/ed). Ice-shelf basal melting
 1134 in a global finite-element sea-ice/ice-shelf/ocean model. *Annals of Glaciology*,
 1135 *53*(60), 303–314. doi: 10.3189/2012AoG60A156

- 1136 Umlauf, L., Arneborg, L., Hofmeister, R., & Burchard, H. (2010). Entrainment
1137 in Shallow Rotating Gravity Currents: A Modeling Study. *Journal of Physical*
1138 *Oceanography*, *40*(8), 1819–1834. doi: 10.1175/2010JPO4367.1
- 1139 Umlauf, L., & Burchard, H. (2005). Second-order turbulence closure models for geo-
1140 physical boundary layers. A review of recent work. *Continental Shelf Research*,
1141 *25*(7), 795–827. doi: 10.1016/j.csr.2004.08.004
- 1142 Vallis, G. K. (1992). Mechanisms and Parameterizations of Geostrophic Adjustment
1143 and a Variational Approach to Balanced Flow. *Journal of the Atmospheric Sci-*
1144 *ences*, *49*(13), 1144–1160. doi: 10.1175/1520-0469(1992)049<1144:MAPOGA>2
1145 .0.CO;2